ELSEVIER

Nuclear Instruments and Methods in Physics Research A 486 (2002) 663–707

NUCLEAR INSTRUMENTS & METHODS IN PHYSICS RESEARCH Section A

www.elsevier.com/locate/nima

The MACRO detector at Gran Sasso

M. Ambrosio[a], R. Antolini[b], R. Assiro[c], G. Auriemma[d,1], D. Bakari[e,f], A. Baldini[g], G.C. Barbarino[a], E. Barbarito[h], B.C. Barish[i], G. Battistoni[j,2], Y. Becherini[e], R. Bellotti[h], C. Bemporad[g], P. Bernardini[c,*], H. Bilokon[j], V. Bisi[k], C. Bloise[j], E. Bottazzi[e], C. Bower[l], M. Brigida[h], S. Bussino[m], F. Cafagna[h], M. Calicchio[h], D. Campana[a], A. Candela[b], M. Carboni[j], S. Cecchini[e,3], F. Cei[g], A. Ceres[h], V. Chiarella[j], B.C. Choudhary[i], S. Coutu[i,4], M. Cozzi[e], P. Creti[c], G. De Cataldo[h], L. Degli Esposti[e], H. Dekhissi[e,f], C. De Marzo[h], I. De Mitri[c], J. Derkaoui[e,f], M. De Vincenzi[m], A. Di Credico[b], D. Di Ferdinando[e], R. Diotallevi[d], O. Erriquez[h], C. Favuzzi[h], C. Forti[j], P. Fusco[h], M. Gebhard[l], G. Giacomelli[e], R. Giacomelli[e], G. Giannini[g,5], N. Giglietto[h], M. Giorgini[e], R. Giuliani[g,i], M. Goretti[i], M. Grassi[g], H. Grau[i], L. Gray[b], A. Grillo[b], F. Guarino[a], C. Gustavino[b], A. Habig[l,6], J. Hanson[i], K. Hanson[p,7], A. Hawthorne[l], R. Heinz[l], J.T. Hong[i], E. Iarocci[j,8], E. Katsavounidis[i,9], I. Katsavounidis[i], E. Kearns[n], H. Kim[i], S. Kyriazopoulou[i], E. Lamanna[d,10], C. Lane[o], A. Leone[c], D.S. Levin[p], P. Lipari[d], G. Liu[i], R. Liu[i], N.P. Longley[i,11], M.J. Longo[p], F. Loparco[h], F. Maaroufi[e,f], G. Mancarella[c], G. Mandrioli[e], S. Manzoor[e,12], V. Marrelli[i], A. Margiotta[e], A. Marini[j], D. Martello[c], A. Marzari-Chiesa[k], M.N. Mazziotta[h], D.G. Michael[i], S. Mikheyev[b,i,13], L. Miller[l,14,✠], P. Monacelli[q], M. Mongelli[h], T. Montaruli[h],

*Corresponding authors. Tel.: +39-0832-320443; fax: +39-0832-325128.

E-mail addresses: paolo.bernardini@le.infn.it (P. Bernardini), peck@hep.caltech.edu (C.W. Peck).

[1] Also at Università della Basilicata, 85100 Potenza, Italy.

[2] Also at INFN Milano, 20133 Milano, Italy.

[3] Also at Istituto TESRE/CNR, 40129 Bologna, Italy.

[4] Currently at Department of Physics, Pennsylvania State University, University Park, PA 16802, USA.

[5] Also at Università di Trieste and INFN, 34100 Trieste, Italy.

[6] Also at Dipartimento di Scienze e Tecnologie Avanzate, Università del Piemonte Orientale, Alessandria, Italy.

[7] Currently at Bartol Research Institute, University of Delaware, Newark, DE 19716, USA.

[8] Also at Dipartimento di Energetica, Università di Roma, 00185 Roma, Italy.

[9] Also at Dept. of Physics, MIT, Cambridge, MA 02139, USA.

[10] Also at Dipartimento di Fisica dell'Università della Calabria, Rende (Cosenza), Italy.

[11] Currently at Macalester College, Department of Physics and Astr., St. Paul, MN 55105, USA.

[12] Also at RPD, PINSTECH, P.O. Nilore, Islamabad, Pakistan.

[13] Currently at Institute for Nuclear Research, Russian Academy of Science, 117312 Moscow, Russia.

[14] Also at Department of Physics, James Madison University, Harrisonburg, VA 22807, USA.

✠ Deceased.

PII: S0168-9002(01)02169-6

M. Monteno[k], L. Mossbarger[i], S. Mufson[l], J. Musser[l], D. Nicolò[g], R. Nolty[i], C. Okada[n], M. Orsini[b,i], C. Orth[n], G. Osteria[a], M. Ouchrif[e,f], O. Palamara[b], S. Parlati[i], V. Patera[j], L. Patrizii[e], R. Pazzi[g], C.W. Peck[i,*], G. Pellizzoni[m], M. Perchiazzi[h], L. Perrone[c], J. Petrakis[l], S. Petrera[q], N. Pignatano[i], C. Pinto[c], P. Pistilli[m], V. Popa[e,15], A. Rainò[h], J. Reynoldson[b], F. Ronga[j], A. Rrhioua[e,f], A. Sacchetti[h], P. Saggese[i], C. Satriano[d,1], L. Satta[j], E. Scapparone[b], K. Scholberg[i,9], A. Sciubba[j,8], P. Serra[e], M. Sioli[e], G. Sirri[e], M. Sitta[k,6], S. Sondergaard[i], P. Spinelli[h], M. Spinetti[j], M. Spurio[e], S. Stalio[g,i], R. Steinberg[o], J.L. Stone[n], L.R. Sulak[n], A. Surdo[c], G. Tarlè[p], V. Togo[e], M. Vakili[r,16], C. Valieri[e], C.W. Walter[i,n], R. Webb[r], N. Zaccheo[b,i]

[a] *Dipartimento di Fisica dell'Università di Napoli and INFN, 80125 Napoli, Italy*
[b] *Laboratori Nazionali del Gran Sasso dell'INFN, 67010 Assergi (L'Aquila), Italy*
[c] *Dipartimento di Fisica dell'Università di Lecce and INFN, via per Arnesano, 73100 Lecce, Italy*
[d] *Dipartimento di Fisica dell'Università di Roma "La Sapienza" and INFN, 00185 Roma, Italy*
[e] *Dipartimento di Fisica dell'Università di Bologna and INFN, 40126 Bologna, Italy*
[f] *L.P.T.P., Faculty of Sciences, University Mohamed I, B.P. 524 Oujda, Morocco*
[g] *Dipartimento di Fisica dell'Università di Pisa and INFN, 56010 Pisa,Italy*
[h] *Dipartimento di Fisica dell'Università di Bari and INFN, 70126 Bari, Italy*
[i] *California Institute of Technology, Pasadena, CA 91125, USA*
[j] *Laboratori Nazionali di Frascati dell'INFN, 00044 Frascati (Roma), Italy*
[k] *Dipartimento di Fisica Sperimentale dell'Università di Torino and INFN, 10125 Torino, Italy*
[l] *Depts. of Physics and of Astronomy, Indiana University, Bloomington, IN 47405, USA*
[m] *Dipartimento di Fisica dell'Università di Roma Tre and INFN Sezione Roma Tre, 00146 Roma, Italy*
[n] *Physics Department, Boston University, Boston, MA 02215, USA*
[o] *Department of Physics, Drexel University, Philadelphia, PA 19104, USA*
[p] *Department of Physics, University of Michigan, Ann Arbor, MI 48109, USA*
[q] *Dipartimento di Fisica dell'Università dell'Aquila and INFN, 67100 L'Aquila, Italy*
[r] *Physics Department, Texas A&M University, College Station, TX 77843, USA*

The MACRO collaboration

Received 6 August 2001; received in revised form 26 October 2001; accepted 30 October 2001

Abstract

MACRO was an experiment that ran in the Laboratori Nazionali del Gran Sasso from 1988 to 2000. Its principal goal was to observe magnetic monopoles or set significantly lower experimental flux limits than had been previously available in the velocity range from about $\beta = 10^{-4}$ to unity. In addition it made a variety of other observations. Examples are: setting flux limits on other so far unobserved particles such as nuclearites and lightly ionizing particles, searching for WIMP annihilations in the Earth and the Sun and for neutrino bursts from stellar collapses in or near our Galaxy, and making measurements relevant to high energy muon and neutrino astronomy and of the flux of up-going muons as a function of nadir angle showing evidence for neutrino oscillations.

The apparatus consisted of three principal types of detectors: liquid scintillator counters, limited streamer tubes, and nuclear track etch detectors. In addition, over part of its area it contained a transition radiation detector. The general design philosophy emphasized redundancy and complementarity. This paper describes the technical aspects of the

[15] Also at Institute for Space Sciences, 76900 Bucharest, Romania.
[16] Also at Resonance Photonics, Markham, Ont., Canada.

complete MACRO detector, its operational performance, and the techniques used to calibrate it and verify its proper operation. It supplements a previously published paper which described the first portion of the detector that was built and operated.

PACS: 29; 29.40.Gx; 29.40.Mc; 14.80.Hv

Keywords: Astroparticle physics; Underground detectors

1. Introduction

MACRO was a large area multipurpose underground detector located at the Laboratori Nazionali del Gran Sasso (LNGS) in Italy. It was designed to search for rare events in the cosmic radiation and it was particularly optimized for sensitivity to the supermassive magnetic monopoles predicted by Grand Unified Theories of the electroweak and strong interactions. Over the years, the collaboration published the results of several monopole searches [1–5]. The experiment could also perform many other interesting searches and precision measurements in various other areas of particle physics, cosmic ray physics, and astrophysics. These included: study [6,7] of both high energy ($\bar{E}_\nu \sim 100$ GeV) and lower energy ($\bar{E}_\nu \sim 4$ GeV) atmospheric neutrinos showing evidence of flavor oscillations [8]; high energy neutrino astronomy [9] and muon astronomy [10,11]; searches for WIMP annihilations in the Earth and Sun [12]; search for low energy ($E_\nu \gtrsim 7$ MeV) stellar collapse neutrinos and antineutrinos [13,14]; studies of various aspects of the high energy underground muons that provide an indirect tool to study the primary cosmic ray composition, origin, and interactions [15,16]; and searches for various conjectured types of matter, as yet unseen, that may exist in the cosmic radiation and contribute to cold dark matter such as fractionally charged particles [17,18] and nuclearites [19]. Over the years the experiment published results on these topics, helping to fulfill the promise inherent in the development of the unique, large experimental halls deep underground at the Gran Sasso Laboratory. Early descriptions of the experiment and its apparatus are given in Refs. [20–22].

At this laboratory, the minimum rock overburden is 3150 hg cm^{-2}. A muon needs a minimum energy of $\simeq 1.3$ TeV at the surface to penetrate this heavy shield and reach the underground laboratory. The cosmic radiation results in a muon flux of ~ 1 m^{-2} h^{-1} in the laboratory with an average muon residual energy of ~ 310 GeV [16].

The apparatus was built and equipped with electronics starting in 1988 and was completed in November 1995. Some data were taken with the partially completed detector between 1989 and 1995, but from November 1995 until May 2000 it ran in its completed, full configuration; from May 2000 to December 2000, a subset of the detector's electronics was used primarily to measure the flux of upgoing muons but the search for slow monopoles was turned off. A previous paper [20], referred to in the following as "I", described the first 1/12 of MACRO and plans for the full apparatus. This is a supplement to that paper, and so reference to it will be made for unchanged details of the apparatus; the emphasis in this paper is on differences between the 1992 description and the actual final detector as well as issues relating to calibration and performance verification.

A glossary of the many acronyms used in this paper is given at its end.

2. General configuration of the detector

The detector had a modular structure: it was divided into six $12.6 \times 12 \times 9.3$ m^3 sections referred to as *supermodules* (SM), each with separate structure and electronics readout. The detector's global dimensions were $76.5 \times 12 \times 9.3$ m^3, its total mass was ~ 5300 t, and its total acceptance to an isotropic flux of particles was $\sim 10,000$ m^2 sr.

Redundancy and complementarity were the primary goals in designing the experiment. Since we could not reasonably expect more than a few monopoles during its lifetime, we deemed multiple signatures and the ability to perform cross checks among various parts of the apparatus as crucial. To accomplish this, the principal detector consisted of three independent sub-detectors: liquid scintillation counters, limited streamer tubes, and nuclear track ("track-etch") detectors.

Fig. 1 illustrates the general layout of the experiment. It shows the six SMs as well as the separation of the detector into a lower half (the *lower detector*) and an upper half (the "*attico*"). Fig. 2 gives a cross-sectional view of the detector. Each of the six SMs contained a total of 77 scintillation counters divided into three horizontal planes (top, center, and bottom) and two vertical planes (east and west). In addition, the two end SMs contained vertical planes covering the lower part of their north and south faces. The lower detector had 10 horizontal planes of streamer tubes, separated by either crushed rock absorbers or (at its top and bottom) a plane of scintillator counters. The total thickness of the crushed rock was $\simeq 420$ g cm^{-2} setting an energy threshold of ~ 1 GeV for a typical muon to pass through the lower detector. Each of its vertical sides had six planes of streamer tubes, separated into groups of three, with a plane of scintillator between them. The attico had two side walls of streamer tubes and scintillator planes, similar to that of the lower detector. Its top consisted of four horizontal planes of streamer tubes separated into two groups with a plane of scintillation counters between them. The attico's central region was mostly open space, housing the readout electronics, some transition radiation detectors and an assortment of work benches and storage cabinets. The details of the attico are described below.

Because of the crushed rock absorbers, the lower detector contained most of the total detector mass (~ 4700 t). Since there was relatively little material in the attico, it was a good approximation to treat it as empty space when considering the stopping power of ionizing particles. Within a supermodule, the horizontal planes of scintillators and streamer tubes were approximately hermetic, with neighboring counters in each SM plane pushed together, but, between the SMs, a vertical gap was necessary for structural support provided mostly by steel I-beams. On the roof of the attico,

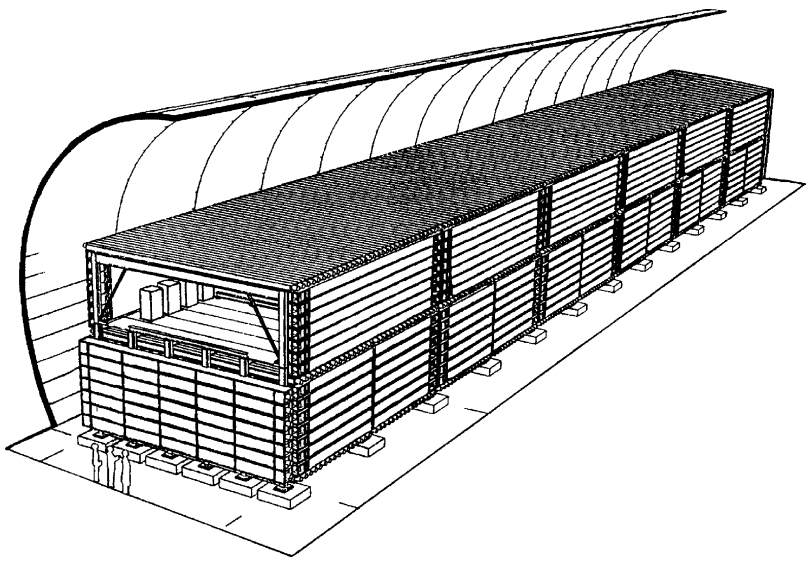

Fig. 1. General layout of the detector installed in Hall B of the LNGS. Overall dimensions of the active part were 76.5 m long, 12 m wide, and 9.3 m high.

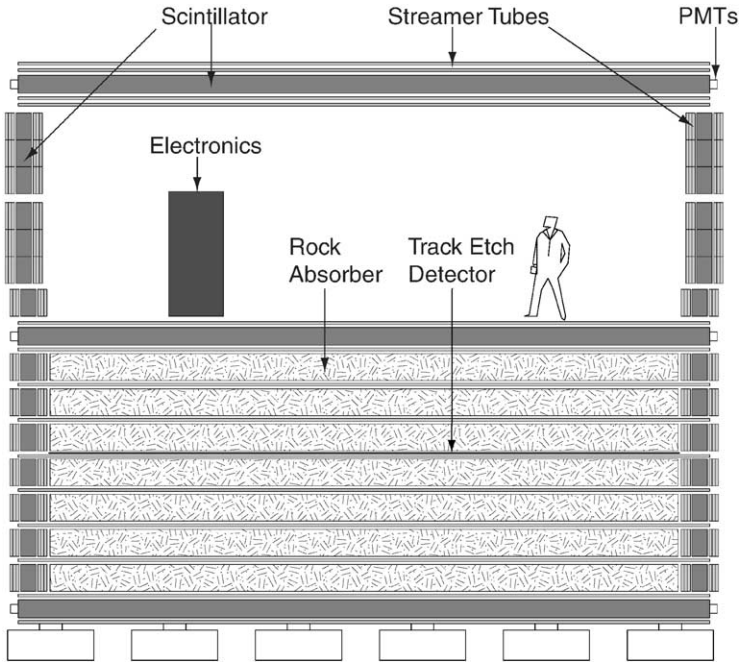

Fig. 2. A cross-sectional view of the detector showing the layout of streamer tubes, scintillation counters, track-etch detectors, and rock absorbers. In addition (not shown), there were vertical planes of track-etch detector just outside the main apparatus on one side and one end, and transition radiation detectors in part of the attico.

however, the horizontal layers of streamer tubes and scintillation counters were contiguous with no gaps between SMs. Also, the vertical planes of streamer tubes and scintillators had gaps (about 15% of the total area) for structural support. All components of the detector, including rock absorber, liquid scintillator, plastic in scintillator tanks and streamer tube walls and structural steel, have been included in the calculation of the total detector mass and have been reproduced in detail in simulations of the detector's response to ionizing particles.

The limited Streamer Tube (ST) system consisted of $\sim 50,000$ tubes, each having a 3×3 cm^2 cross-section and a length of 12 m. The tubes were filled with a gas mixture of 73% He and 27% *n*-pentane. Signals were detected on anode wires on all planes. On horizontal planes a second coordinate readout was provided by pick-up strips below the chambers at an angle of 26.5°. The intrinsic position and tracking resolutions of the streamer tube system were ~ 1 cm on the wire view and $\sim 0.2°$ on the strip view, but the overall angular resolution for cosmic ray muons was limited to $\sim 1°$ by the multiple Coulomb scattering in the rock around the detector.

The nuclear track-etch detector was deployed in three planes, horizontally in the center of the lower detector and vertically on the east and north faces. The detector was divided into 18,126 individual stacks which could be individually extracted, etched, and replaced as needed. Each stack had dimensions $24.5 \times 24.5 \times 0.65$ cm^3 and was composed of three layers of CR39, three layers of Lexan and 1 mm of aluminum absorber to stop nuclear fragments.

Details of the scintillator system, streamer tube system, and track-etch are given in Sections 3, 4 and 5 respectively.

In addition to the three detection elements already described, a Transition Radiation Detector (TRD) was installed in part of the attico, directly above the central horizontal plane of the detector. It was composed of three individual

modules (overall dimensions $6 \times 6 \times 2$ m^3), made of 10 cm thick polyethylene foam radiators and proportional counters. Each TRD counter measured $6 \times 6 \times 600$ cm^3 and was filled with 90% Ar and 10% CO_2. The TRD provided a measurement of the muon energy in the range of $100\ \text{GeV} < E < 930\ \text{GeV}$. Its energy measurement saturated at ~ 930 GeV but muons of higher energies were still detected and identified. Details of this system are given in Section 6.

Since the attico's construction was somewhat different from that of the lower detector and it was not described in I, its details are given here. It consisted of two vertical walls and a top cover immediately above the lower detector; its dimensions were $76.5 \times 12 \times 3.5$ m^3. As noted above, the roof of the attico, being contiguous, was more hermetic than the lower detector at the cost of less modularity for the detector. For data acquisition and triggering the modularity was enlarged to a Double Supermodule (DSM) that corresponded to one μVax computer in the data acquisition system. Nonetheless, some vestiges remained of the lower detector's segmentation into supermodules. As in the ST planes of the lower detector, the attico detectors were divided into vertical and horizontal planes. The vertical faces were equipped with six ST planes and one plane of scintillator counters, as in the lower detector. The attico roof was composed of four ST planes and one scintillation counter plane as shown in Fig. 3. A 5 cm polystyrene foam spacer was inserted between each pair of horizontal ST planes to improve the tracking capability of the attico roof. As in the lower detector, all attico ST horizontal planes were equipped with pick-up strips allowing the determination of the second coordinate in each plane. Unlike the lower detector, the attico vertical planes were equipped with 5.5 cm wide strips (pitch 6.0 cm) at right angles to the ST wires, while the strips on the roof horizontal planes were 3.1 cm wide (pitch 3.25 cm) at a 26.5° stereo angle. Although the strip width in the vertical planes was about twice that used in the horizontal ones, this choice did not degrade the angular resolution of the tracking system because of its 90° stereo angle.

3. The scintillator system

The scintillation counters and their performance are fully described in I and so only a short description, for completeness, will be given here. The discussion will describe the final waveform digitizing system (WFD) used in the experiment, the various triggers produced by the scintillator system, and the methods used to verify the proper operation of the system and its calibration.

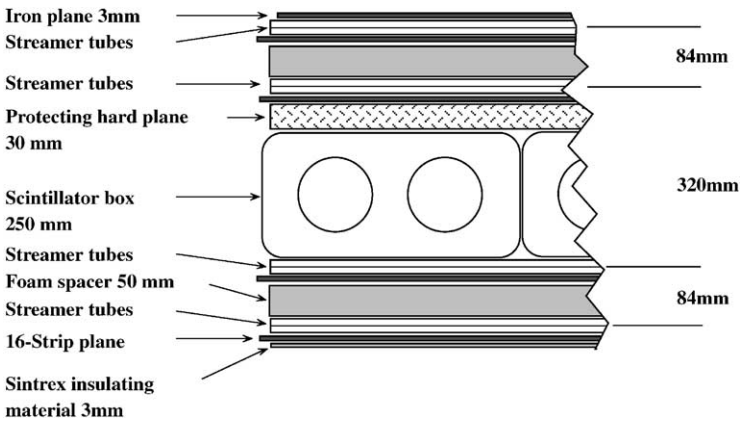

Fig. 3. End view of one scintillator counter in the horizontal layer of the attico roof showing relative locations of the scintillator, the streamer tubes, and the strips.

3.1. The scintillation counters

The counters in the horizontal planes had an active volume of $11.2 \times 0.73 \times 0.19$ m^3, and those in the vertical planes, $11.1 \times 0.22 \times 0.46$ m^3. All were filled with a mixture of 96.4% mineral oil and 3.6% pseudocumene, with an additional 1.44 g l^{-1} of PPO and 1.44 mg l^{-1} of bis-MSB as wavelength shifters. The horizontal counters were viewed by two EMI 8″ photomultiplier tubes (PMTs) at each end and the vertical counters by one 8″ PMT at each end; in the attico, Hamamatsu PMTs were used. Each PMT housing was equipped with a light collecting mirror. The total number of scintillators was 476 (294 horizontal and 182 vertical) with a total active mass of 560 t. The scintillator counter construction for the whole of MACRO was the same as in the first SM.

The signals from the PMTs were reproduced in fast fan-out circuits and distributed to a collection of triggering and measuring electronics described below. Some triggers were formed from single counter signals and others were developed from signals summed over the PMT outputs of collections of geometrically related counters. This provided redundancy in the triggering system, and also allowed specialized triggers to select events firing multiple counters. Measurements were made of the total charge and relative time of occurrence of the signals from each end of each counter in two independent systems, the Energy Response Processor (ERP) and the Pulse Height Recorder and Synchronous Encoder (PHRASE). Both of these systems are fully described in I and, except for the addition of a subsystem to measure the time between the TDC stop signals for the ERPs in different SMs, the systems finally used were essentially unchanged from those descriptions; they will not be further detailed here. In addition, however, for almost all events, the full waveforms of the PMT signals were measured with 5 ns sampling for amplitudes below a saturation limit set by either the PMT or the fan-out circuit. This measuring system is described below in Section 3.2. In addition the portion of the PMT waveform below 255 mV was also recorded in the PHRASE electronics.

A minimum ionizing muon crossing a horizontal counter vertically had a most probable energy loss of $\sim$34 MeV in 19 cm of scintillator; if it passed equidistant from the ends, it produced about 600 photoelectrons in each. No deterioration in the scintillator performance was observed in about 10 years of operation. Overall, the scintillator system's timing and longitudinal position measurements on single particles in a counter had resolutions of $\sim$0.5 ns and $\sim$10 cm respectively.

3.2. Waveform digitizer

One of the most powerful signatures of a rare event in a scintillator counter is the waveform of the PMT signals it produces. Thus, in a search for rare events in a large scintillator system, digitization of the PMT waveforms with high resolution and good fidelity is essential. It allows background rejection in searches for monopoles, nuclearites, and lightly ionizing particles, and it also provides a powerful alternative to ADCs and TDCs for charge and time measurement.

The experiment utilized a custom built, common-stop waveform digitizer (WFD) to record these signals. Amplitude digitizations were made and stored continuously until a stop signal, suitably delayed after an event, interrupted the process, freezing the memory. Its most important intended use was to observe the transit of a slow monopole crossing a scintillator. For example, a monopole moving vertically with velocity $\beta = v/c = 0.7 \times 10^{-3}$ yields a square pulse 1 μs long with photoelectron statistical fluctuations superimposed. An LED simulation of such a signal containing the expected number of photoelectrons for a magnetic monopole (about 5000) is shown in Fig. 4(b). This WFD replaced a small number of LeCroy 2261 CCD-based digitizers used during the experiment's early stages.

The WFD had a flow-through design. An input analog PMT signal fed both a voltage discriminator and a non-linear amplifier. The discriminator triggered when the input was outside the range $\pm$2.5 mV and the amplifier output was digitized by a flash ADC (FADC) at a 200 MHz rate. The bipolar sensitivity of the trigger was very important to avoid misinterpreting small, bipolar,

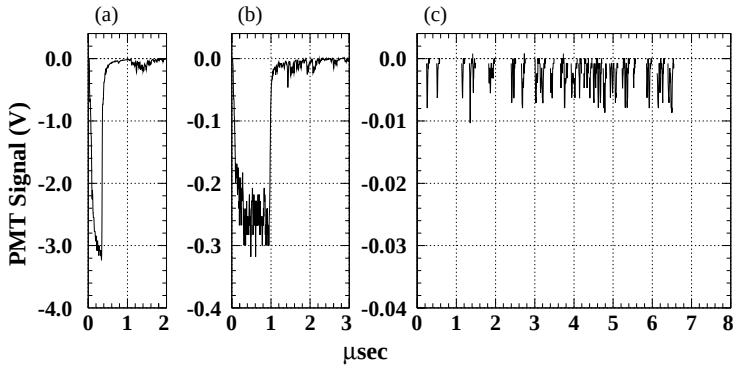

Fig. 4. LED simulations of monopole signals for velocities of $\beta = 2 \times 10^{-3}$(a), 7×10^{-4}(b), and 1×10^{-4}(c). The systematic change in the photoelectron rate is an LED artifact and would not occur for a monopole.

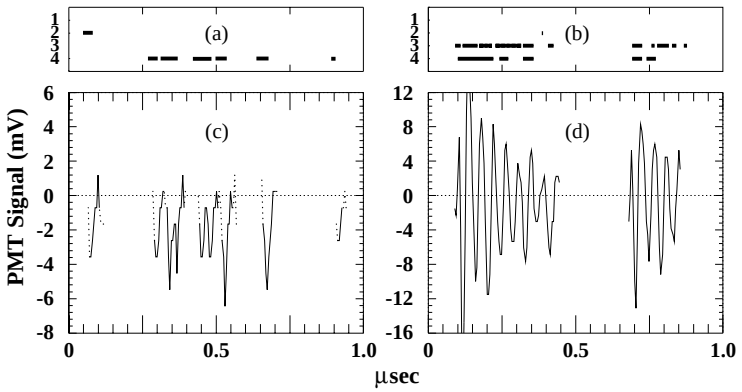

Fig. 5. This figure shows two examples of waveform outputs for low level signals, one an interesting signal (c) produced by an LED fired just at the SMT threshold, and the other, (d), electrical noise.

oscillatory noise bursts as trains of negative pulses, mimicking sequences of single photoelectron pulses. Examples of both an interesting signal and bipolar noise are shown in Fig. 5(c) and (d) respectively. Further, voltage measurements were made within a 20 ns range of a trigger so parts of a pulse not satisfying the trigger condition were also captured; this is shown by the dotted parts of Fig. 5(c). When the recording process was stopped by external signals, the RAM was readout through the VME backplane by the data acquisition system. Fig. 6 shows an overview of one WFD board.

The important features of the design and their motivating requirements are as follows:

200 MHz clock speed. The narrow pulse width (15 to 20 ns) of the scintillation counters required a system that had a sampling rate of about 5 ns. Very slow monopoles are expected to register distinctive trains of single photoelectron pulses, typically 12 ns FWHM. Fig. 4(c) shows a sequence of single photoelectron signals.

64 kbyte/channel memory. Because monopoles of interest could take up to 1 ms to traverse the detector, a deep memory buffer with a maximum size of 64 kbyte was used to store the waveform data. This allowed full reconstruction of events in which a GUT monopole catalyzed nucleon decay as it approached the detector; with a shorter recording time, relativistic nucleon decay products could pretrigger the detector and cut off the information about the passage of the monopole. Because of software limitations, we actually used

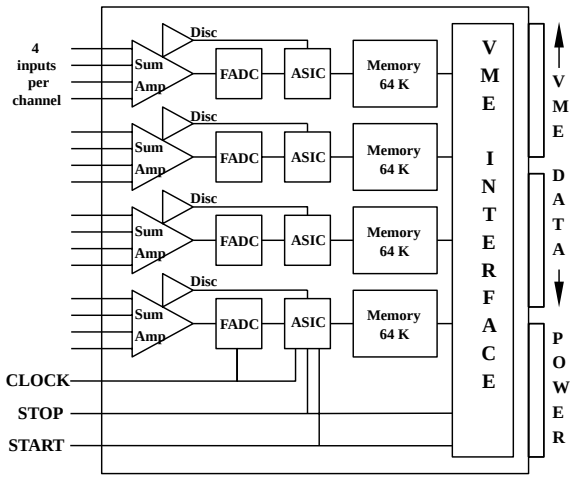

Fig. 6. A diagrammatic side view of one WFD board.

only 50 kbyte of the available buffer, and some initial running was with even smaller buffer sizes. In monopole searches, these limitations were taken into account. The memory used allowed up to 128 μs of PMT signal history to be recorded; typically only ~15% of this was used.

Hardware zero suppression. Hardware zero suppression was implemented so that only the waveform data for which a discriminator had been triggered within 20 ns were recorded. This limited the amount of data to a manageable size, and also allowed the measurement of waveform details for short times both before and after a discriminator had fired, as shown in Fig. 5(c).

Customized multiplexing. We implemented multiplexing of four PMT signals into one digitizer channel. However, each PMT signal was individually discriminated and 4-bits were associated with each sample of the recorded waveform to identify the channel(s) contributing to it, as shown in Fig. 5(a) and (b).

Non-linear front-end amplifier. Since single photoelectron pulses had an average amplitude of −4 mV, a high-gain input amplifier was required. On the other hand, the PMTs could produce signals as large as −10 V, requiring attenuation. This wide dynamic range of about 4000 was handled by a non-linear front-end amplifier, with a small-signal differential gain of 10 and a large-signal differential attenuation of 10, smoothly mapping the input range into the 8-bit linear range of the FADC.

VME packaging. The backplane interface was designed to the IEEE 1014-1987 version of the VME bus standard to allow for rapid transfer of the memory buffer to the data acquisition system. We used the 9U package to provide sufficient board space for the many components.

There were three external control signals: CLOCK, STOP, and START. A 200 MHz CLOCK was produced in a central location and fanned out to each WFD card. The WFD Stop Master (WSM), which generated the STOP signal, received inputs from almost all the triggers within a supermodule as well as the ORs of some triggers from adjacent SMs as described below. To allow measurement of both the entry and exit pulses of a slow monopole, the WSM normally produced the STOP signal after a delay of 1 ms from the earliest occurring trigger. In addition, when more than one supermodule produced its own WFD-stopping trigger, the WSM also measured the relative time of all of them with a 10 MHz clock. VME readout took place after the WFD was stopped. Finally, after readout, the data acquisition system produced a START signal to put the system back into recording operation.

For each digitization channel, four PMT signal inputs were processed by one front-end amplifier and summed into a single analog output signal. Each of the four input signals was separately discriminated. These logic signals identified which of the inputs contributed to the summed analog signal and they also controlled zero suppression. The summed signal was digitized by an AD9028 8-bit FADC (8 mV bit^{-1}) clocked at 200 MHz. Since, as noted above, the non-linear input circuit amplified small signals by 10 times and attenuated large signals by the same factor, the resolution was 0.8 and 80 mV bit^{-1} for small and large signals respectively. The response of the circuit is illustrated in Fig. 7. Tests showed that this response was stable to about 2% at an input of −2 V.

Each channel was equipped with a custom Vitesse Application Specific Integrated Circuit (ASIC) which assembled the digital data, appearing once every 5 ns from the FADC and the discriminators, into parallel format and stored

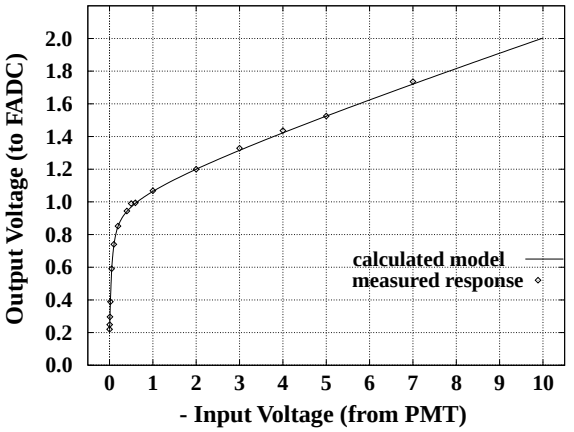

Fig. 7. The measured response of the WFD non-linear input amplifier compared with a mathematical model for the circuit.

four such pairs in registers. If any of the discriminator bits in these four samples had been set, the data in the registers together with a 16 bit time word were transferred into the RAM memory at an address generated by the ASIC. Thus some recorded voltage measurements were within the ± 2.5 mV range of the discriminators. This process continued until receipt of a STOP from the WSM which caused all of the waveform channels in a supermodule to be simultaneously stopped. Subsequently, selective readout of WFD channels was controlled by software. Based upon the contents of trigger registers which were readout by the data acquisition system, a complete list of hit scintillators was generated to control the WFD readout routines.

The support hardware consisted of six 9U VME crates each holding 10 or 11 WFD boards and serving one SM. The configuration of the board was software controlled. It was possible to enable or disable zero suppression and to set the discriminator thresholds to values different from the normal ± 2.5 mV. In addition, software could write test patterns to memory to verify proper operation of the read-outs.

3.3. Scintillator triggers

The electronics for the scintillation counters provided specific triggers for various rare particles, minimum ionizing particles, and gravitational collapse neutrinos. Each SM had its own complement of triggers as described below and auxiliary circuits were provided to connect adjacent SMs when necessary.

MACRO's general purpose trigger circuit was the ERP which used TDCs and ADCs to provide triggering, timing, and charge measurement for PMT pulses corresponding to energy losses in the scintillator as low as 7 MeV. Furthermore it could integrate the PMT pulse from a monopole as slow as $10^{-2}c$. Finally, it had provisions for detecting a burst of gravitational collapse neutrinos. This circuit was fully described in I and so its design and implementation are not discussed here.

An independent system, the Pulse Height Recorder and Synchronous Encoder (PHRASE), was particularly adapted for the detection of gravitational collapse neutrinos but it also had functional capabilities similar to the ERP. Again, this circuit and its operation were fully described in I and are not repeated here.

With its special emphasis on the search for slowly moving magnetic monopoles, the experiment employed a specially designed Slow Monopole Trigger (SMT), sensitive to monopoles with velocities from about 10^{-4} to $10^{-2}c$. As with other triggering circuits, it was described in I but, because implementation changes were made for the attico, it is discussed here in Section 3.3.1.

For monopoles in the velocity range from about 5×10^{-3} to $5 \times 10^{-2}c$, the PMT signals were easily detected by conventional voltage discriminators and these were used to produce a Fast Monopole Trigger (FMT). Fig. 4(a) shows an example of an LED simulated signal of a monopole with velocity $\beta = 2 \times 10^{-3}$. It contains about $\sim 17,000$ photoelectrons, and also shows an afterpulse about 1 μs after the primary signal. The FMT and other specialized triggers are discussed in Sections 3.3.2–3.3.5.

Finally, after the first supermodule was built, MACRO was equipped with a special trigger for Lightly Ionizing Particles (LIP). It was sensitive to fractionally charged particles down to about $e/5$ and is described in detail in Section 3.3.6 below.

3.3.1. The Slow Monopole Trigger (SMT)

Magnetic monopoles can exist in nature over a wide spectrum of velocities with respect to Earth and, correspondingly, they can have a wide range of transit times and light yields in scintillators. For monopoles traversing the detector with typical galactic ($10^{-3}c$) or solar system ($10^{-4}c$) velocities, scintillator signals will be a wide pulse of small amplitude or a train of single photoelectron pulses lasting several microseconds. An LED simulation of the expected signal from a monopole with $\beta = 1 \times 10^{-4}$ is shown in Fig. 4(c); the single photoelectron train contains only ~ 70 photoelectrons. In order to trigger on such a signature, the SMT was developed for MACRO. Its philosophy and implementation for the first supermodule are discussed in detail in I. Briefly, it consisted of two parts:

- an analog circuit which translates an input PMT pulse into a TTL pulse whose duration was nominally the time that the input pulse amplitude exceeded half its maximum. It was called the Time-Over-Half-Maximum (TOHM) circuit.
- a digital circuit consisting of a scaler which counted up at a fixed frequency (66 MHz) when the TOHM output was high and at a lower frequency, software settable, when the TOHM output was low. It was called the Leaky Integrator (LI) circuit.

An SMT pretrigger occurred when the LI scaler for the signal coming from one end of a scintillator counter reached a predetermined count. This typically was 11, corresponding to a signal with width $\geqslant 180$ ns. A coincidence within 20 μs between pretriggers from the two ends of one scintillator produced an SMT trigger.

Each PMT signal in the detector had a dedicated TOHM and LI channel, but there were two versions of hardware. The older version was built with DIP silicon components and was used in all of the lower detector; there were 72 TOHM NIM modules and 276 LI CAMAC modules accommodating the 552 PMT signals. Its installation was completed in December 1992. The 400 scintillator signals from the attico and the north and south faces used a version of the SMT hardware constructed from surface mount silicon components and field programmable gate arrays. Packing density was increased by more than a factor of five so that only 14 CAMAC modules accommodated the 400 signals. The installation of this version of the SMT hardware was finished in November 1995. Both versions of the SMT hardware featured selectable PMT threshold (settable by CAMAC command in the attico circuits and manually in the others) and CAMAC adjustable triggering criteria for the LI. The threshold was normally set to -2 mV.

The SMT circuit for a SM triggered its WSM to stop its WFD system and also identified the triggering scintillators to direct the data acquisition system's readout circuits. Further, SMT signals were supplied to adjacent SMs so that their WSMs could provide auxiliary timing information connecting monopole-like signals in different SMs, if there were any.

3.3.2. The Fast Particle Trigger (FPT)

The FPT provided a trigger for particles with $\beta > 3 \times 10^{-2}$ and its principal function was to produce a veto for the Fast Monopole Trigger (see below). For this trigger, eight horizontal or seven vertical scintillators were treated as a single *supercounter*. The several PMT signals from each end of a supercounter were analog summed and amplitude discriminated at a level corresponding to about 1/6 of a typical muon signal. The discriminator outputs from each end of a supercounter were then put into 100 ns coincidence. The digital outputs from all the end-to-end coincidences of supercounters belonging to one face of a supermodule were ORed together and used to produce a 1 μs face pulse. Finally the overlap of two or more such face pulses from a single SM or a pair of adjacent ones produced the FPT. In addition, this system provided the data acquisition system with a register which recorded the supercounters producing the coincidence. It did *not* directly trigger the WSM and so it did not force the production of waveform information. In fact, however, the vast majority of events selected by the FPT also triggered the ERP system which both triggered the WSM and provided ADC/TDC information.

3.3.3. The Fast Monopole Trigger (FMT)

The FMT was a conventional Time Of Flight (TOF) trigger for the detection of magnetic monopoles of intermediate velocities. Except for its output pulses, it used the same hardware as the FPT muon trigger just described. The FMT circuitry produced $\sim 10\,\mu s$ output pulses rather than $1\,\mu s$ ones for producing two-face coincidences. When an FPT trigger occurred, these signals were vetoed. Thus the FMT selected particles with TOF within the detector between 1 and $10\,\mu s$; for a nominal pathlength of 9 m, this corresponds to a β range of 3×10^{-2} to 3×10^{-3}. The FMT was input to the WSM and so it caused waveforms to be recorded.

3.3.4. The Highly Ionizing Particle Trigger (HIPT)

The most energetic events triggering either the FPT or the FMT were automatically flagged for the data acquisition system by the Highly Ionizing Particle Trigger (HIPT). This circuit attenuated the FPT supercounter signals by a factor of 10. They were then discriminated at levels corresponding ~ 1.7 times the typical minimum ionizing signal (0.2 V for the horizontals and 0.14 V for the verticals). Except that its output pulse was $10\,\mu s$ long, the subsequent logic was then the same as that for the FPT. Like the FMT, the HIPT triggered the WSM and so waveform information was collected for the supercounters involved.

3.3.5. The High Charge Trigger (HCT)

Because of residual gas in the PMTs, their normal signals were followed after about $1\,\mu s$ by a relatively large afterpulse, as can be seen in Fig. 4(a), followed by a train of single photoelectron afterpulses. The initial rate of these single photoelectrons was roughly proportional to the charge in the initiating PMT signal and it decayed to a quiescent value over times of hundreds of microseconds. This phenomenon occurs even with the intrinsic residual gas in a new PMT, but is exacerbated by helium buildup as a tube ages. The helium used by the ST system diffused through the streamer tubes' thin plastic walls, and so the atmosphere in the MACRO experimental hall had a higher helium concentration than the normal atmosphere. This gas subsequently diffused through the PMT glass envelopes, increasing the PMT residual pressure and the size and duration of the afterpulsing. The afterpulse trains following very high-charge PMT signals, such as those expected from nuclearites or fast monopoles, could saturate the finite-depth WFD memory and this would result in the loss of the originating pulse. Furthermore, abnormally large inputs produced capacitive coupling overshoots exceeding the WFD $+2.5$ mV threshold and these also could cause memory saturation. As noted above, the WFD stop was normally produced about 1 ms following the occurrence of a trigger but for large signals this time had to be reduced to avoid completely filling the memory.

The HCT was produced by integrating the FPT supercounter signals and triggering at a $10\,V\,\mu s$ threshold; this corresponded to a charge of ~ 100 times that of a muon. To prevent loss of the WFD data from the originating pulse, the HCT produced a WFD STOP signal after a delay of just $120\,\mu s$. This time window was just below the maximum that completely filled the 50 kbyte of waveform memory when a WFD digitized continuously. Since all WFD channels within a single supermodule were stopped simultaneously, a particle with $\beta < 10^{-4}$, satisfying this trigger, did not have the waveform in the scintillator from which it exited the detector recorded by the WFD. This was a necessary compromise; it was essential that the WFDs record single photoelectron pulses and the PMTs themselves suffered from this intrinsic afterpulsing property. However, both the waveform from the entering face and the TOF information from the scintillator system were recorded.

3.3.6. The Low Ionizing Particle (LIP) trigger

The LIP trigger was designed to be sensitive to penetrating particles whose energy loss in the scintillators was as small as 1/25 that of a minimum ionizing muon. Its general philosophy was to be sensitive to very small signals from the scintillators and to maintain the overall trigger rate at an acceptable level by requiring a multiple coincidence including streamer tubes.

For scintillator inputs, this trigger used signals from the lowest energy-based discriminators available in the experiment. These were in the PHRASE system which suitably combined signals from both ends of a scintillator to correct for light attenuation in the scintillator; they triggered on an energy loss greater than ~ 1.2 MeV anywhere in a scintillator. To make these available to the LIP circuits, the PHRASE units were modified relative to the configuration originally used in the first SM.

The LIP circuit itself was a digital, clocked, synchronous system. It operated at 5 MHz and was based upon two XILINX field-programmable gate array chips, an XC3090 and a smaller XC3020. These were controlled by an inexpensive 16K PROM, the XILINX XC1765. Its general logic configuration is shown schematically in Fig. 8.

After the inputs were synchronized to the LIP clock, they were ORed into three logical faces for each SM: top (including all of the attico scintillators), center (the horizontal layer between the attico and the lower detector), and bottom (all the other scintillators in the lower detector). In addition, to allow the LIP to trigger on particles passing between SMs, the OR of half of each layer was passed to the LIP circuits in the adjacent SMs.

A scintillator pretrigger for LIP was a coincidence with resolution of ~ 400 ns either between all three logical layers in a SM or between two layers in one SM and one in another. In this latter case, a pretrigger was formed in both SMs independently. Pretriggers latched scintillator firing information into a register for subsequent readout if all the trigger conditions were satisfied. At the low discrimination level used, the triggering rate from a single scintillator, due primarily to radioactivity, was ~ 2–3 kHz, yielding a pretrigger rate of several per second per supermodule. If this had been recorded, it would have saturated both the data acquisition and the storage systems. Thus, to reduce the rate to an acceptable level, a coincidence with a signal from the ST system was required. To allow time for ion propagation in the streamer tubes, the LIP logic waited 6.4 μs for an ST trigger. If one occurred, the LIP trigger was produced and fed to the supermodule's WSM; otherwise, the latches were cleared and the circuit once again became sensitive to scintillator coincidences.

In data analysis, the charge and relative time of the scintillator signals that produced the trigger were obtained from the recorded waveforms rather

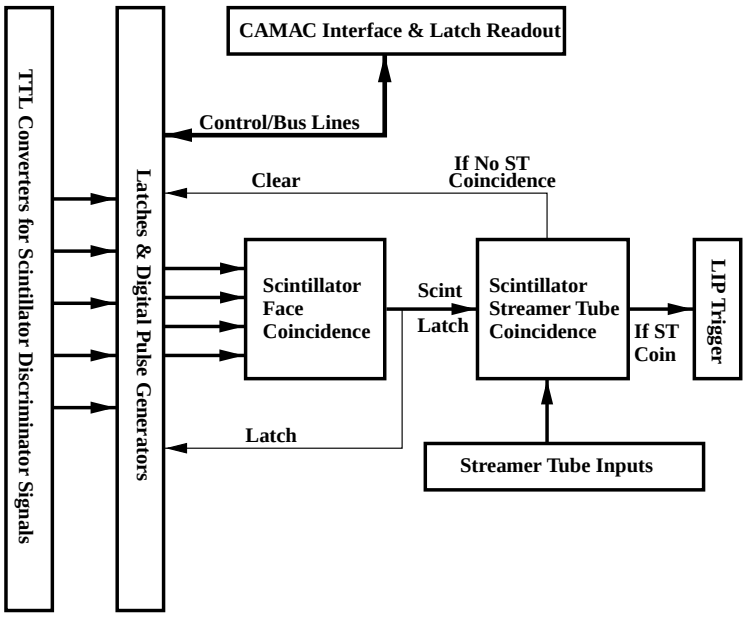

Fig. 8. A schematic of the LIP trigger circuit logic.

than from a traditional ADC/TDC system. This technique strongly suppresses an especially dangerous source of accidental background in a LIP search to which some ADC/TDC systems are susceptible: a small radioactivity pulse can start an ADC/TDC gate just prior to the arrival of a normal minimum ionizing signal. If the integration gate closes during the normal signal, this can occasionally result in the reconstruction of an event with a much smaller energy than actually deposited in the scintillator. Use of the detailed waveforms in the analysis avoided this problem.

3.4. Performance verification and calibrations

With its large complement of triggers and measuring electronics, the scintillator system needed convenient equipment and procedures to detect malfunctions, allowing timely repairs, and to regularly provide parameters for converting measured quantities (e.g., ADC or TDC counts) to physical quantities (e.g., MeV of energy loss or nanoseconds relative delay). Three different sources were used to provide this information: nitrogen lasers which simultaneously pulsed light into the longitudinal center of each scintillator in a group via optical fibers, LEDs mounted near each PMT which could be excited individually, and the signals produced by penetrating muons themselves. For details on the laser system and the LEDs, see I. The procedure used to convert the raw ADC and TDC signals produced by the ERPs to physics quantities is described in Sections 3.4.1 and 3.4.2. It depended upon linearity of the PMTs, the fanouts, and the ADC/TDC channels and this was regularly verified by special calibration runs in which the laser and LEDs were excited with parameters systematically varied. The relative laser signal amplitude was controlled with a precision optical attenuator and was also measured with special monitor PMTs and electronics. Similarly, the LEDs were pulsed with precision time delays relative to a measured common trigger pulse, and with precisely set amplitudes and pulse widths. Thus it was possible to test the SMT with good facsimiles of the light signals expected from magnetic monopoles of any velocity within our range of interest. We also created facsimiles of the extraordinary events which should trigger the FMT and HCT. In addition, we used the LEDs to test the capability of the ERP and PHRASE GC triggers to detect a neutrino burst from a stellar gravitational collapse by producing a scatter of many low-energy events distributed over the whole apparatus during a suitable time interval. Approximately once a month, every scintillator in the system was excited by each of these test patterns and the data analyzed immediately. Thus we regularly verified that essentially all of the triggering system was functioning as designed and, for the relatively small portions of the system in which problems arose (a few counters typically), we took corrective actions. This system proved to be highly effective for verifying and maintaining the proper operation of the experiment.

3.4.1. ERP energy calibrations

A principal task for the ERP system was to measure the energy deposited in each scintillator by physics events and of particular interest was the energy range of neutrinos from a stellar gravitational collapse (~ 5–~ 50 MeV). The procedure used for energy reconstruction depended upon a set of nine constants for each counter: a gain G_i and a pedestal p_i for each end of the counter, $i = 0, 1$, and a five-parameter function describing light attenuation as a function of position in the scintillator; as described below, these parameters were determined regularly for each counter. For light levels up to those produced by muons, it was shown in I that the PMT charge, measured by the ERP ADC circuit, was proportional to the number of photoelectrons to a good approximation. Thus for an event j, we reconstructed a quantity $w_{j,i}$ that was proportional to the number of photoelectrons from end i:

$$w_{j,i} = G_i(\mathrm{ADC}_{j,i} - p_i) \quad (1)$$

where $\mathrm{ADC}_{j,i}$ is the number of counts measured by the ADC, p_i is the pedestal, and G_i is a gain factor initially set at a convenient value and subsequently adjusted as described below to track variations in the system gain for each channel. The value of $w_{j,i}$ was then converted into an energy measurement

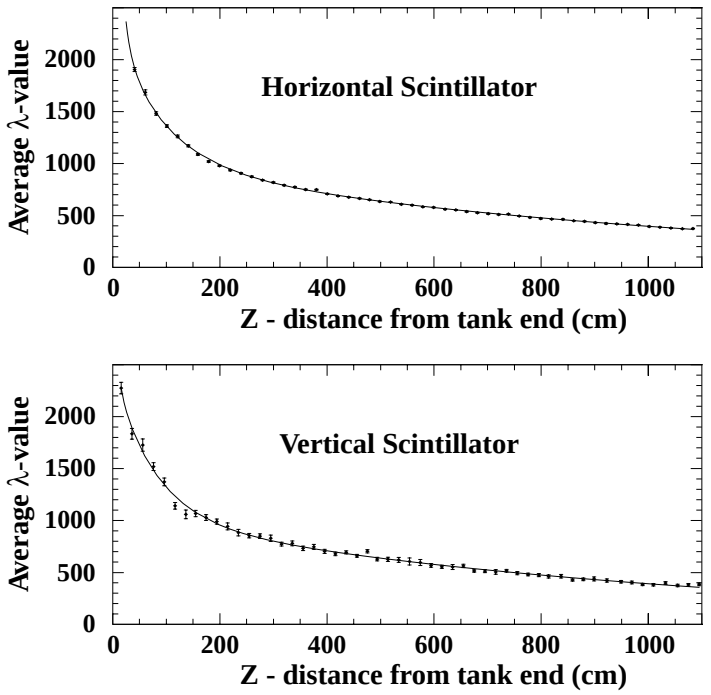

Fig. 9. ERP muon response data and their fit to the form of Eq. (3). In this figure, the points shown are averages of groups of four of the directly determined λ-values.

according to

$$E_{j,i} = w_{j,i}/R(Z_{j,i}) = \left(\frac{G_i}{R(Z_{j,i})}\right)(\mathrm{ADC}_{j,i} - p_i) \qquad (2)$$

where $R(Z_{j,i})$ gives the light attenuation factor for the event j occurring a distance $Z_{j,i}$ from end i; it was scaled to convert w-values into energy. This response function for a scintillator was approximated by

$$R(Z) = A\exp(-Z/B) + C\exp(-Z/D) + E/Z^2 \quad (3)$$

where the constants A, B, C, D, E were counter-dependent and taken to be the same for both ends. Fig. 9 shows typical examples from the horizontal and vertical scintillators. Finally, a weighted average of the energy measurements from the two ends was taken as the reconstructed energy:[17]

$$E = \frac{E_0\sqrt{w_0} + E_1\sqrt{w_1}}{\sqrt{w_0} + \sqrt{w_1}}. \qquad (4)$$

The first step in the calibration procedure was to determine the pedestals p_i. The laser system injected light at the center of each scintillator at several different levels determined by a variable light attenuator in the laser beam. Approximately 100 pulses were fired at each light level starting at or below the ERP trigger threshold (corresponding to $\sim$5–6 MeV) and extending up to the muon level ($\sim$34 MeV). One monitor PMT viewed a constant light signal from the laser to produce triggers, and another, the reference PMT, measured the attenuated light so that its pulse charge was proportional to the amount of light sent to the counters. This charge was digitized by a linear reference ADC, whose pedestal was determined independently. For each side of each scintillator and for each attenuator setting, the pedestal-subtracted reference ADC values and ERP ADC values were averaged. The ERP averages were then linearly fit

[17] A statistically optimal energy resolution is obtained with a weighted average $E = (E_0\mu_0 + E_1\mu_1)/(\mu_0 + \mu_1)$, where μ_i is the mean number of photoelectrons reaching end i for an ensemble of events. However, the resolution improvement with respect to formula 4 is not significant in this experiment. In MACRO software the formula 4 was used for historical reasons.

to the reference averages. The intercept of this fit determined the ERP pedestal. Fig. 10 shows an example of a laser pedestal fit for one side of one counter.

A carefully selected sample of muon events, the *muon calibration sample*, was used to determine both the gain parameters G_i and the parameters in the light attenuation function in Eq. (3). Using the streamer tube system, we chose events containing just one, non-showering muon with a well determined trajectory. From the muon's trajectory, its Z position in a counter was determined and the values $w_{j,i}$ were calculated using the newly determined pedestals and the values of G_i from the previous calibration. Initially, values of G_i were selected so that the average w-value for muons passing through the longitudinal center of a counter was 600, approximately the number of photoelectrons produced by these signals. Each counter was divided into 5 cm longitudinal bins, and the three parameters N, α, λ (normalization, width, and location) in the function $NL(\alpha(w-\lambda))$ were least-squares fit to the distribution of w-values observed in each bin; $L(x)$ is the well-known Landau function,

$$L(x) = \frac{1}{2\pi \mathrm{i}} \int_{c-\mathrm{i}\infty}^{c+\mathrm{i}\infty} \mathrm{e}^{px+p\log p}\, \mathrm{d}p, \quad c \geqslant 0. \tag{5}$$

Finally, the function $\lambda(Z)$ was fit using Eq. (3) to obtain the five response function parameters for each counter; the same function was used for both ends of a counter. This procedure was adopted since this fitting function well approximates the shape of the observed w-distribution and its location measure, λ, is statistically robust.

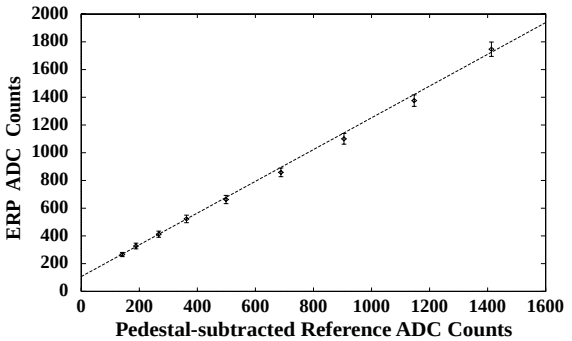

Fig. 10. Typical linear fit of the ERP ADC counts to the reference ADC counts for determining the ADC pedestals.

Lastly, the gain constants G_i were adjusted to set the energy scale. For each event, a first approximation to the energy loss in each counter was calculated from Eq. (2) using G_i values from the previous calibration and the newly determined response function $R(Z)$. Each muon's pathlength through scintillator oil in each counter was calculated from the ST trajectory, and finally, values of the gains G_i were adjusted so that the distribution of the fully corrected energy divided by pathlength, fitted to the Landau function as described above (with w replaced by energy/pathlength), produced a λ value of 1.8 MeV/cm to within $\pm 2\%$. An example of such a fit is shown in Fig. 11.

This procedure and energy normalization are not rigorously correct since the actual distribution of the energy loss per unit pathlength for our scintillators is the Landau distribution (with theoretically determined values of the parameters α and λ) folded into photoelectron statistics and pathlength uncertainties. However, allowing the width-setting parameter α to be adjustable is a convenient way to approximate the distribution broadening due to these two effects. Similarly, fixing the value of λ is a good approximation to the true situation in which its value weakly depends on the number of photoelectrons and the pathlength. Detailed studies which used the full Landau theory of the energy-loss distribution folded with these broadening effects showed that the procedure used gave an energy normalization systematically too large by $\sim 5\%$ with an overall uncertainty of about the same size. Since no physics using these calibrations was sensitive to the energy loss in a counter at the 5% level, no correction was included to accommodate this small systematic error.

The gains and pedestals for the ERP attenuated-ADC values were determined in the same way as for the unattenuated values. The ERP attenuated-ADC input signal was reduced by a nominal factor of 10 with respect to the unattenuated value and was used for pulses with very large charge. Over much of the range of the attenuated-ADC, the system response was non-linear, and when ERP

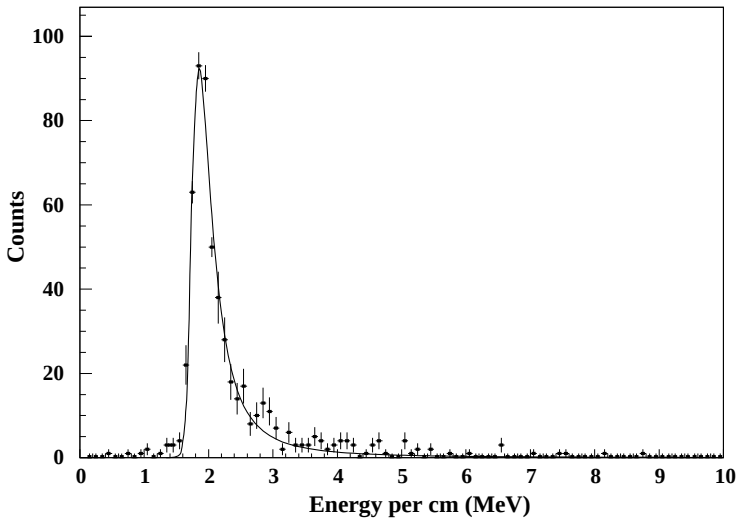

Fig. 11. Typical distribution of energy loss divided by pathlength from a muon calibration sample. Also shown is the Landau function with least-square adjusted normalization, width, and location parameters as described in the text.

measurements based upon them were used, special calibrations were necessary. These are described in Refs. [2,5]. The ERP attenuated-ADCs were never used in searches for stellar gravitational collapse events.

3.4.2. ERP timing calibrations

Several of the physics analyses that could be performed with MACRO required precise timing in the scintillator system. Some examples are:

- the position of an event along the longitudinal axis of the scintillator could be determined from the relative timing of signals at its two ends. Neutrinos from supernovas should be distributed uniformly throughout the scintillator volume, so the gravitational collapse analysis compared the position of events determined by timing to a uniform distribution to rule out anomalies of either the GC trigger or other hardware.
- the TOF of particles between two scintillators. This was the only way the neutrino-induced upgoing muon signal (~ 0.5 event per day) could be distinguished from the downgoing muon background ($\sim 10^4$ events per day).
- additional tracking information for muon events which stop or originate in the detector triggering very few planes of the ST system.

The ERP was a common-stop system with fixed voltage-level amplitude discriminators to mark times. A constant current was gated into an integrator, starting when a PMT pulse exceeded the amplitude discriminator level. The gate was closed by a stop pulse, which was common for all of the scintillators in one SM. Subsequently, the voltage on the integrator was converted into the digital TDC value.

For each scintillator, the time $t_{j,i}$ at which the light pulse for event j arrives at scintillator end i relative to an arbitrary event time, unique for each SM, was reconstructed as

$$t_{j,i} = t_i^{\text{off}} - r_i\left(\text{TDC}_{j,i} + \frac{\alpha_i}{\sqrt{\text{ADC}_{j,i}}} + \frac{\beta_i}{\text{ADC}_{j,i}}\right). \tag{6}$$

In this equation, t_i^{off}, r_i, α_i, and β_i are parameters for each end of each scintillator. An offset time, governed by PMT delays, cable lengths, and electronic delays, was accommodated by t_i^{off} and the conversion factor from TDC counts to time

was r_i. The terms in α_i and β_i provide an approximate timewalk correction to account for the fact that the TDCs measured time from the moment that the input signal exceeded a fixed threshold value rather than from the moment a pulse starts. Thus, for two pulses starting at the same time, the one with the smaller amplitude will cross threshold later, starting the TDC later.

The reconstructed times $t_{j,i}$ can also be expressed in terms of the time t_j at which the scintillation occurred in the scintillator and the distance of the scintillation from the center of the counter, z_j:

$$t_{j,0} = t_j + \left(\frac{L}{2} + z_j\right)\frac{n}{c}, \tag{7}$$

$$t_{j,1} = t_j + \left(\frac{L}{2} - z_j\right)\frac{n}{c}. \tag{8}$$

The two parameters, L and c/n, in these equations are the length of a scintillator and the effective propagation velocity of light along its longitudinal axis, respectively; they are the same for both ends of a counter. The lengths of the scintillators are taken as known but the light velocity parameter n was regularly determined to accommodate the possibility of slow chemical changes in the scintillator oil (none was observed). These last two equations are trivially solved to yield

$$z_j = \frac{1}{2}(t_{j,0} - t_{j,1})\frac{c}{n}, \tag{9}$$

$$t_j = \frac{1}{2}(t_{j,0} + t_{j,1}) - \frac{L}{2}\frac{n}{c}. \tag{10}$$

The procedure to determine the several parameters in the above equations utilized the same set of laser pulses described above for finding the ERP ADC pedestals, the same muon calibration sample, and data from specialized LED calibration runs.

The laser system was configured so that the laser pulse, suitably delayed, created the ERP common stop and so measuring the change in TDC values as the phototube pulse height was varied allowed the parameters α_i and β_i to be determined.

The special LED calibration runs used a programmable pulser which allowed setting precision delays between the LED excitation signals and a trigger pulse; the trigger pulse, again suitably delayed, provided the ERP common stop time. These LED data were used to determine the r_i parameters.

The muon calibration sample was used to determine the time offsets, t_i^{off} and the light velocity parameter, n. First, n and $(t_0^{\text{off}} - t_1^{\text{off}})$ for each counter were adjusted so that a linear fit of the z_j values determined from Eq. (9) to those determined by the streamer tube system yielded a unit slope and zero intercept. Then, the relative offsets between scintillators were determined by making a second pass through the muon calibration sample, reconstructing the TOF of particles between scintillators using the ST tracking data, and assuming all the particles were downgoing and relativistic. An iterative process was used; starting with the offset times determined in the most recent previous calibration, the average measured value of $1/\beta$ for particles striking a particular scintillator was determined. If this was not unity to within the statistical precision of the mean (about one part in 20,000), the offsets were adjusted. This change, of course, affected the TOF measured between this scintillator and other scintillators, and so new β determinations were then made, and the process was continued until it converged.

The ERP common stop was different for each SM. To determine the TOF for particles that crossed supermodule boundaries, a stand-alone TDC was used to measure the time between common stops on different SMs. The slopes and offsets of this TDC were determined in a multi-parameter fit which minimized the difference between expected TOF and measured TOF, again utilizing events in the muon calibration sample.

One way to measure the timing resolution of the scintillator system for muons is to compare the longitudinal position in a scintillator reconstructed from timing to that reconstructed by the streamer tube system. Summed over all scintillators in the apparatus, the central part of the distribution of the difference is almost a Gaussian with a standard deviation of 10.4 cm and a mean of less than 1 cm. This implies that a scintillator's timing resolution was about 0.5 ns which is consistent with the central Gaussian peak in the TOF measurements of muons.

3.4.3. The WFD system

Since the WFD system was based upon a highly non-linear amplifier, it was necessary to carefully demonstrate its performance in all of the energy ranges in which it was used. To do this, several calibrations and checks on this system were performed. Low intensity LED pulses were used to demonstrate its sensitivity to single photoelectron pulses; ambient radioactivity was used to confirm and calibrate its sensitivity at low energies; cosmic ray muons were used to calibrate its response in the medium energy range by comparison against the ERP; and high light level LED pulses were used to calibrate its sensitivity to large pulses at and above the trigger point of the HCT.

For slow monopole detection, in which the expected PMT response was a sequence of single photoelectron pulses, the most important role of the WFD was pattern recognition. Accurate energy reconstruction for such an event was not required; the waveforms were simply used to distinguish a single photoelectron sequence from bipolar electronic noise, and to get an estimate of the TOF across a single scintillator. Thus to confirm WFD sensitivity to slow monopoles it was sufficient to generate low light events using LEDs; examples are given in Figs. 4 and 5 above. This was done weekly when the efficiency of the slow monopole scintillator trigger was measured.

For the fractionally charged particle search more refined calibrations were required. For energies below 5 MeV we used the natural background radiation to calibrate the WFD response. Since 1 ms of data were stored in the WFDs for muon events, which typically leave a PMT active for a few microseconds at most, there was an abundance of radioactivity waveforms during our normal running for use in this kind of calibration. Care was taken to avoid using data contaminated by PMT afterpulsing. An energy spectrum was obtained for each counter and the most prominent peaks were assumed to originate from the potassium line at 1.46 MeV and the thallium line at 2.61 MeV. By comparing these lines to measured background spectra in the MACRO hall, and to Monte Carlo simulation of the scintillator response for background radioactivity events, low energy calibrations were obtained for most scintillator counters as shown in Fig. 12. For further information see Refs. [17,18].

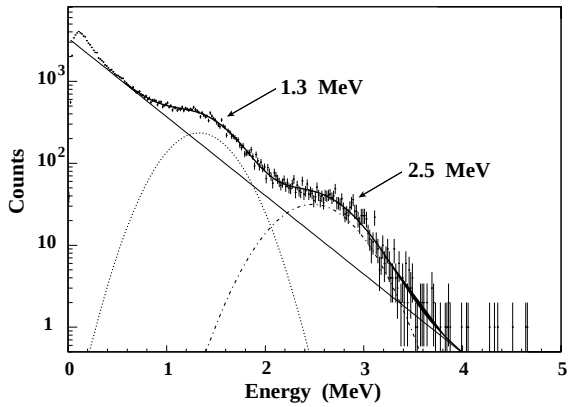

Fig. 12. A typical low energy spectrum observed in the horizontal counters with the WFD. The two peaks correspond to the 1.46 MeV potassium line and the 2.61 MeV thallium line. The peaks are shifted slightly because of smearing from other decay components in the spectra.

For moderate energy events near 40 MeV, cosmic ray muons were the primary tool for verifying WFD response. Fig. 13 shows two examples of muon signals. As for the ERP, the muon calibration sample was regularly used to calibrate the WFD data. By computing the WFD-determined energy loss per unit path length as a function of the longitudinal position of the particle in the scintillator, we verified that we reproduced the known scintillator response function for each scintillator. This method provided another calibrated energy point for the LIP analysis. Simply comparing the WFD integrated charge to ERP ADC value on an event by event basis for each scintillator end gave another verification of the WFD response in the muon energy range. By verifying linearity between the WFD and the ERP responses as shown in Fig. 14 we confirmed that the WFDs were behaving as expected for muons.

Since large amounts of deposited energy are expected from fast monopoles, dyons, and nuclearites, it was also important to confirm that the WFD system was sensitive to very large signals. When the WFD system was initially installed, it was found that large signals could exceed its memory capacity because of small positive overshoots due to capacitive coupling triggering the

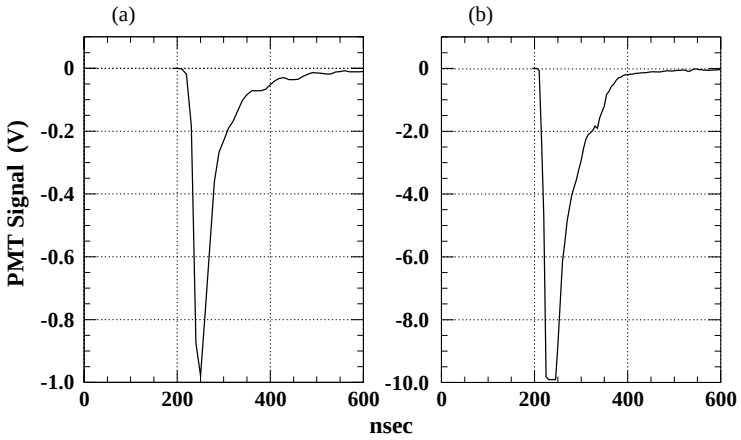

Fig. 13. Two examples of the system's response to muons as shown by the WFDs. In (a) a muon passed through the counter far from the PMT, while in (b) one passed very near the PMT, showing the hard saturation of the analog system at 10 V.

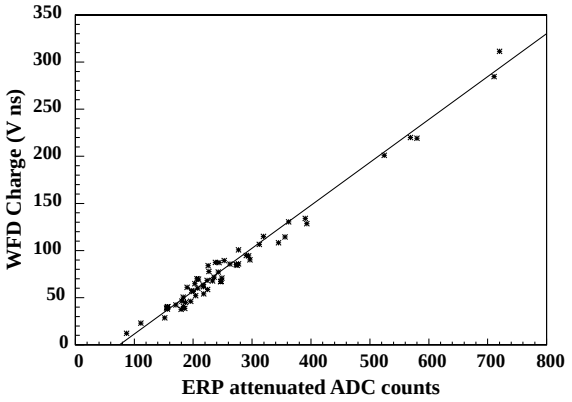

Fig. 14. Comparison of WFD charge to ERP attenuated-ADC for muons passing through a scintillator. The line is to guide the eye.

discriminator and because of the long duration of PMT activity following a highly ionizing event. Most occurrences of the overshoot problem were corrected by suitable circuit modifications and the residual, by the HCT trigger circuit described in Section 3.3.5. Subsequently we routinely verified that pulses at the PMT saturation level were retained by the WFD system. An example of a saturating muon pulse is given in Fig. 13(b).

Together all of these calibrations and checks confirmed that the WFD responded well to all light levels of interest in this experiment and we verified that it was an effective tool for seeking both low energy rare events and highly ionizing events such as those expected from fast monopoles, dyons, and nuclearites.

3.4.4. SMT performance verification

In order to investigate the overall performance of the SMT, a detector-wide test of the triggering efficiency for each individual SMT circuit was first performed in February 1996 and subsequently became part of the normal apparatus performance verification. The detector's LED system was used to perform this test. The LED at one end of a scintillator was pulsed for durations varying from 350 ns to 6.5 μs and amplitudes were adjusted so that the PMT nearer the LED always received enough light to give an SMT pretrigger and the PMT at the other end was excited by a few single photoelectrons. Figs. 4 and 5(a) discussed above show examples of the LED simulated monopole signals used.

Varying the LED amplitude varies the number of single photoelectrons at the far PMT and so allowed the pretrigger efficiency of the far scintillator end to be mapped from zero to 100%. Each time the LED was fired, the WFD was read out from both ends of the scintillator whether or not a pretrigger occurred. The waveforms from each event were analyzed and a simulation in software of the function of both the TOHM and LI parts of the SMT circuitry was performed. This allowed an

a priori determination (i.e., independent of the SMT) of the number of times the SMT circuit should have triggered. The ratio of the observed number of SMT triggers to the number determined by the waveform analysis yielded the SMT efficiency for each scintillator counter. A typical efficiency graph obtained in this way is shown in Fig. 15, in which we plot the efficiency of the SMT circuit as a function of the number of LI counts in the waveform analysis.

Using the clock rates of the LI, we translate the 99% efficiency point into the light yield necessary to trigger the SMT as a function of particle velocity. Fig. 16 shows the measured light yield (normalized to that of a minimum ionizing particle) required for the SMT to achieve 99% triggering efficiency in a typical scintillator as a function of particle velocity. In the same plot, the light yield for bare monopoles with a single Dirac charge [1] is also shown. These results are for almost all the scintillators in the detector (for various reasons, measurements could not be made on $\sim 5\%$ of the scintillators).

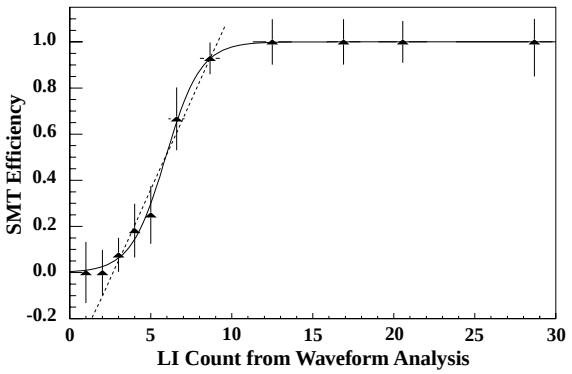

Fig. 15. Efficiency plot of a typical SMT circuit as a function of the number of the LI counts produced by the waveform analysis. This SMT circuit demonstrates 100% efficiency above its nominal threshold which was 10 LI counts corresponding to a signal duration of $\geqslant 180$ ns.

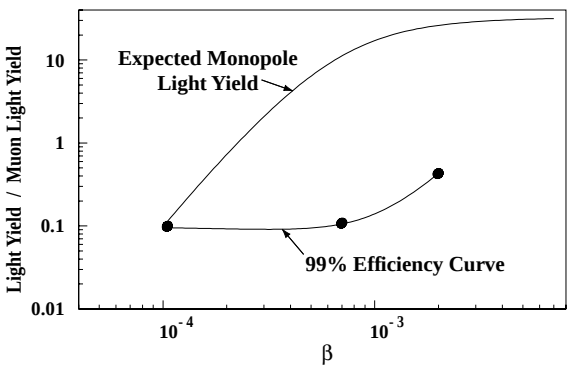

Fig. 16. SMT sensitivity curve as measured with the LED method described in the text. A particle with light yield above the efficiency curve has more than a 99% probability to trigger the SMT.

3.4.5. *FPT/FMT/HIPT/HCT verifications*

Roughly once a month, the LED calibration system was used to check the performance of the FPT, FMT and HIPT circuitry. LED firings in different detector planes with variable delays (from 0 ns to 11 μs) were used to verify the design performance of the triggers. Moreover, variable LED pulse height settings were used to create PMT pulses ranging from below threshold all the way up to saturation for verifying the threshold settings of the triggers. This calibration program insured that the sensitivity of the MACRO experiment was always maintained at its design value.

4. The streamer tube system

The description of the plastic streamer tubes (STs) as the basis of the tracking system was extensively reported in Refs. [20,22], and references therein and so we give only a brief description here. The basic unit of the tube system was a 3.2 cm × 25 cm × 12 m chamber containing eight individual cells, each of dimension $2.9 \times 2.7\ \text{cm}^2$. The silvered Be–Cu anode wire in the center of the cell had a diameter of 100 μm. Three sides of the cell were coated with low-resistivity graphite ($<1\ \text{k}\Omega\ \text{square}^{-1}$) to perform the cathode function by the electrode-less shaping principle [23]. This structure was inserted inside an uncoated PVC envelope (1.5 mm thick) and closed by two plastic end caps. The full detector had 6192 chambers in operation, for a total number of 49,536 wires.

A gas mixture of He (73%) and *n*-pentane (27%) was used in order to exploit the

Drell–Penning effect [24] for slow monopole detection. The gas volume of the active elements was 465 m^3 and the gas distribution system normally recirculated the gas mixture to minimize consumption. The tightness of the chambers was tested under low vacuum (1/3 atm) [25] and only a small diffusion occurred for light gases (for 1 atm of helium the measured diffusion rate was $\sim 5 \times 10^{-6}$ atm cm^{-2} s^{-1}). The gas circulation was regulated at a rate of one change of the whole volume per 5 days and the pressure inside the chambers was maintained at a few mbar above atmospheric pressure.

Each wire behaved as a transmission line with a characteristic impedance of 330 Ω and a propagation time of ~ 3.3 ns m^{-1}. Each wire provided a digital readout for tracking; in addition, analog signals from groups of adjacent wires (32 for the horizontal planes and 16 for the vertical) were added and the summed charge was measured and readout. The plastic STs with resistive cathodes allowed a two-coordinate readout [26]: one view was provided by the wires and the other by external pick-up strips. Two different strip systems were used in MACRO as described above.

MACRO STs operated for many years which allows us to draw sound conclusions about their long term performance and reliability and this is detailed in Section 4.1. In the attico, the characteristic impedance of all the strips was optimally matched to the input resistance of the digital readout electronics, as described in Section 4.2. The full detector had a total of 118,848 digital readout channels for the wires and strips, plus 1548 analog readout channels for the wires. Developments and improvements in the ST readout are described in Section 4.3 and a description of the streamer tube trigger systems is given in Section 4.4.

4.1. Operation, reliability and lifetime of the streamer tubes

In MACRO a large number of wires operated for a considerable time period. The need to guarantee a long lifetime for the experiment (it started taking data in 1989 and was active to the end of 2000) necessitated particular care in the fabrication, conditioning and qualification testing of the active detector elements. After the final installation, only 17 out of the 49,536 wires (0.03%) gave no signal because of poor soldering or bad connections in the end caps of the chambers. This careful construction, in addition to the favorable low background rates, allowed the implementation of simple controls and protections. In particular, the experiment reliably operated with a current limit of 10 μA on each individual HV channel supplying 192 wires. The most important remaining factors for providing stable and safe operations were therefore the stability of the gas system and the prevention of gas leaks. Experience showed that discharges, which increased current and wire stress, were associated with air contamination. Thus special care was taken to ensure the tightness of the chambers, including the vacuum tests [25] mentioned above.

Regarding maintenance during the lifetime of the experiment, we replaced a significant fraction of the sections of short PVC gas tubing connecting one chamber to the next due to evident aging. During MACRO's lifetime, only a further 84 wires started to exhibit permanent discharging behavior and so they had to be disconnected. Most of these wires became noisy within one year from the beginning of operation and, since 1995, only 6 wires per year were disconnected. This time constant is characteristic of some tiny residual fabrication defect, practically impossible to analyze. The final fraction of dead channels was 1.70×10^{-3}. These dead channels were almost evenly distributed over the whole detector, although there was some excess in the first SM which had been put into operation in 1988: 21 disconnections in 12 years, 13 of which occurred in the first 3 years of operation.

The most practical method to check the detector's gas mixture and its relative HV working point was to monitor streamer charge and the plateau of the singles counting rate. This was done in a short chamber inserted in series in the gas flow line. Because of the very low radioactivity background, this measurement was performed with a small β source (^{90}Sr) kept in a fixed position over one of the 8 wires of the test chamber. Since the

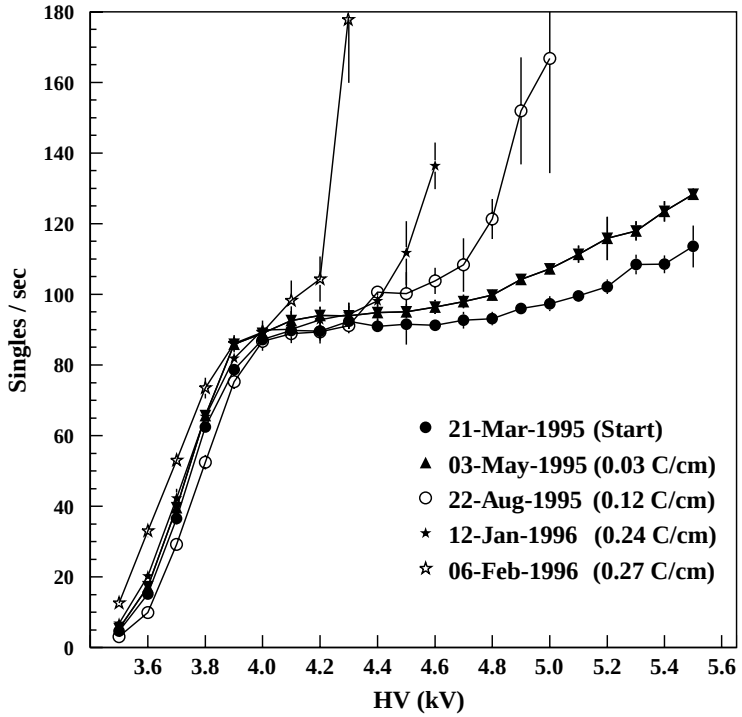

Fig. 17. Singles rate plateau as measured on the test chamber for different values of integrated charge. A localized β source spreading over about 2 cm of wire was used for the measurement.

test chamber was continuously held at the same voltage as the tubes in the full system, the time evolution of the plateau length as a function of the integrated charge allowed us to study the aging effects on the streamer tubes following the same concepts described in Ref. [27]. The β source provided a counting rate of about 90 Hz over 2–3 cm of wire. Each streamer pulse contributed a charge of 200 pC, summing both electron and positive ion components. We therefore integrated about 1.56 mC per day over a couple centimeters of wire. Fig. 17 shows the time evolution of the singles counting rate plateau of a single wire test chamber [28]. The charge and current monitoring in the same test setup has shown that no anomalous effects, like dark current, could be observed at the operating voltage as long as a reasonable counting rate plateau could be observed. Since the tubes were normally operated 200 V above the knee of the plateau, we see that aging with the He + n-pentane gas mixture made a tube inoperable after the integration of about 0.3 C cm^{-1}, i.e., approximately one year for the test chamber. Applied to the underground operation at the Gran Sasso, this aging rate implies completely safe operation over a time much longer than the lifetime of the experiment. In fact, the average counting rate due to the natural background as measured by the STs was $\sim$40 Hz m^{-2} of ST plane, corresponding to 12 mHz cm^{-1} of wire. Therefore, the expected lifetime of tubes was at least 3000 times that of the test chamber. In addition to the monitoring of this test setup, the current drawn by all the different groups of wire on the detector has been monitored for the whole operation period of the apparatus. No appreciable changes in the average values could be observed, as expected.

4.2. The attico strips

In the attico all the STs, both horizontal and vertical, were equipped with pick-up strips. This is a significant improvement compared to the lower

detector described in Refs. [20,22] which had strips only for the horizontal STs. This enhancement permitted full tracking capability using the vertical STs.

The pick-up strips for the horizontal planes of the attico were made using 4 mm thick honeycombed polypropylene foil. The strips were 30 mm wide and the spacing between adjacent ones was 2.5 mm. As in the lower part of MACRO, the pick-up strips were grouped in bands of 16 elements. Laboratory measurements of the properties of these strips showed that the signal attenuation was $0.038\,\mathrm{dB\,m^{-1}}$, the characteristic impedance of a single line was $40 \pm 1\,\Omega$, and the cross talk between neighboring strips, 14.1 m long, was 5%. Each strip was terminated with $39\,\Omega$ impedance to reduce the dependence of pulse amplitude on the streamer location.

The $40\,\Omega$ characteristic impedance of these strips permitted an increase in the threshold of the front end electronics by about a factor 2.5 compared to what was used with the lower detector strips which had a characteristic impedance of only $8\,\Omega$. The efficiency of the attico strip system was 3% higher than the system used in the lower detector.

4.3. Attico wire and strip readout

The acquisition system for attico wire and strip signals used a new and improved version of the STAS (ST Acquisition System) model C267 and of the Splitter Board model SY 480, both produced by CAEN [29]. Because the clock signals issued by a STAS were sent back to the same STAS, this new read-out system was insensitive both to the length of the connection cable to the read-out chain and to the delay introduced by the electronics. The serial output from the chains was acquired from the STAS on the high-to-low transition of acknowledgment signals, thereby synchronizing the data read-out with the STAS clock.

In this new STAS, each channel had its own 512 word FIFO memory and so, in contrast to the model C187 used in the lower detector, no arbitration logic was necessary. This allowed a clock frequency of up to 4 MHz resulting in faster data acquisition. Further, all connections to the Splitter Board were made optically to avoid ground loop problems.

In the lower detector, each read-out chain serviced just one detector plane. In the attico, however, each such chain typically serviced several planes to better exploit the STAS module memory.

For triggering purposes each plane of counters sent a FAST–OR signal to the trigger modules. All the 23 chains used to read out a DSM in the attico fit into three 8-channel Splitter Board units.

4.4. The ST monopole trigger

The streamer tubes provided a monopole trigger completely independent of the scintillator system. To achieve this, helium and *n*-pentane were used in the gas mixture to exploit the Drell–Penning effect [24]. A monopole passing through a helium atom leaves it in an excited metastable state (Drell effect). Excited helium atoms can collide with an *n*-pentane molecule and ionize it (the Penning effect). This sequence provides an efficient process for detecting monopoles in a streamer tube in the velocity range of $10^{-4} \leqslant \beta \leqslant 10^{-3}$. For monopoles of $\beta \geqslant 10^{-3}$, the standard excitation–ionization mechanisms are effective [30].

For $\beta \leqslant 10^{-3}$, the analysis strategy was based on TOF measurements. Due to the large monopole ionization power [30] in the high β region, the limited proportionality of STs [31] allowed us to reject the muon background by measuring and analyzing the charge released in the ST system [32] (see Section 4.5.4). Here we give a general description of the ST magnetic monopole trigger system.

4.4.1. The trigger system

Large temporal windows (hundreds of μs) were needed in order to search for monopoles (or other exotic particles) with β as small as $\sim 3 \times 10^{-5}$. This, in turn, implied the need for good rejection power against the natural radioactivity background ($\sim 40\,\mathrm{Hz\,m^{-2}}$ of ST plane). To achieve this we required alignment of hits in both space and time, as described below.

Two different triggers were implemented, one using signals from the STs of the horizontal planes and the other using those from the vertical planes.

Monte Carlo simulations showed that this trigger configuration provided a large acceptance of about 8500 m^2 sr for an isotropic particle flux.

4.4.2. The horizontal streamer tube trigger

A full description of this trigger (which took data from 1992) was given in Ref. [33]. Because of the ~ 3 m gap between the lowest horizontal plane of the attico and the highest horizontal plane of the lower detector, a trigger using only the lower detector had a better signal to noise ratio than one which incorporated the attico signals also.

A supermassive particle should cross the apparatus with no significant change in its initial direction and speed, thus producing a straight line in the z-time plane, where z is the vertical position in the detector. The trigger algorithm was designed to be sensitive to these space–time tracks. It operated as the OR of 320 delayed coincidences (β-slices) with a resolution of ~ 2 μs each. Half of these β-slices were arranged to detect upgoing particles and the other half, downgoing ones. In this way a rough TOF measurement was also performed.

The trigger circuit achieved this performance using a serial-in/parallel-out, 480 cell shift register driven by a 1 MHz clock, so creating a 480 μs memory depth. Every microsecond, a search was performed among the β-slices for at least one space–time alignment (see Fig. 18) over a minimum number of planes with signals, normally 7. When successful this produced the Low THR trigger. There was also another, more selective trigger that required particles to cross at least 8 planes with TOF $\geqslant 3$ μs; it produced the High THR signal. Its rate was a factor of about 100 smaller than that of Low THR, which enabled it to trigger the scintillator system WSM, and so force acquisition of scintillator waveforms.

There were 11 trigger units creating parallel signals coming from groups of two adjacent central modules. This reduced the accidental coincidence rate to the tolerable level of ~ 0.2 Hz with negligible loss of acceptance.

For sufficiently slow particles (TOF $\geqslant 3$ μs corresponding to $\beta \leqslant 5 \times 10^{-3}$), the circuit gave different outputs for upgoing and downgoing cases. As described below, this was used to provide as much information as possible on each event.

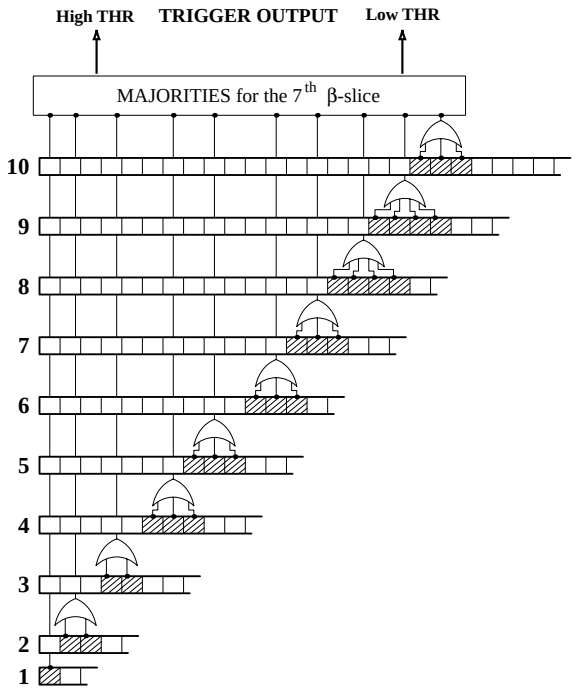

Fig. 18. Simplified scheme of the shift register used by the horizontal streamer tube trigger. Each shift register chain gets signals from one horizontal streamer tube plane. In particular the definition of the 7th β-slice is shown; other β-slices were similarly defined.

4.4.3. The vertical streamer tube trigger

Each of 26 trigger units dealt with signals coming from a single vertical module. The temporal tracking algorithm described above could not be used efficiently in the vertical trigger since a monopole with $\beta \sim 10^{-4}$ would take ~ 30 μs to cross a vertical module. Since the maximum jitter in an ST was $\simeq 600$ ns, its time resolution was insufficient to exploit time alignment in the velocity range of interest. Therefore, only spatial alignment of hits was required with a segmentation of 50 cm along the vertical axis, corresponding to the OR of 16 wires.

The logic required that at least 4 out of 6 planes showed hits within a time window of 45 μs. A stricter coincidence of 9.5 μs was required for signals coming from the inner or the outer planes

separately. In this way, the radioactivity trigger rate was reduced to ~ 0.1 Hz in the whole apparatus.

If the TOF between inner and outer planes was greater than 600 ns, it was also possible by timing to discriminate between particles entering and leaving the apparatus and so produce a corresponding trigger output. Otherwise a *fast monopole* ($\beta \geqslant 3 \times 10^{-3}$) output was produced. There was also a high threshold condition in this circuit. It required at least 5 out of 6 active planes to be hit in coincidence with the same timing as described above. The *slow monopole* output of this logic was used to trigger the WSM, forcing WFD acquisition from the scintillators.

4.4.4. Trigger output management

Management of all the trigger outputs was performed by a suitable streamer monopole supervisor whose function was to store as much information as possible for each individual event. For example, some monopole trajectories could satisfy the trigger conditions before the particle finished crossing the whole apparatus. In this case several hits could have been lost, but this was avoided by using both the ~ 1 ms memory depth of the front-end electronics and the trigger's ability to recognize the direction of slow particles. Proper delay of the data acquisition allowed the collection of all possible information from the event.

The design of this trigger system paid particular attention to the possibility that monopoles might catalyze nucleon decay [34]. By triggering any fast particle trigger, decay products could have caused dead time leading to loss of some, or possibly all, monopole information. To avoid this, the start of event acquisition was delayed by 480 μs to allow time for the monopole to exit the apparatus.

Summarizing, the magnetic monopole trigger of the ST system in the MACRO experiment was sensitive to GUT monopoles with β as small as $\sim 10^{-4}$. Because of this large β range, strong rejection of the hits caused by natural radioactivity was needed and it was obtained by requiring both spatial and temporal tracks. In some circumstances discrimination on the direction of the particle was also possible, allowing preservation of the maximum amount of information, even in the case of a monopole-catalyzed nucleon decay. Two independent triggers were used, one for the horizontal streamer tubes and the other for the vertical ones. Both this configuration and the size of the apparatus allowed a geometrical acceptance of about 8600 m^2 sr for an isotropic particle flux.

4.5. Track reconstruction and performance of the ST system

Large numbers of cosmic ray muons were studied in an effort to assess the overall performance of the ST system. The tracking algorithms, geometrical survey, tracking angular resolution, absolute pointing accuracy, and overall detection sensitivity for these muons are discussed below.

4.5.1. Tracking

The muon tracking procedure was mainly based on the streamer hits of the horizontal planes (central tracking). The track was reconstructed in two views. In the X–Z view (the x axis was that of the gallery) it was reconstructed by means of the streamer tube hits. The inductive pick-up strips permitted the tracking in the D–Z view, where the axis was normal to the strips. With respect to the description in I the tracking package has been further developed. The hits of the North and South frontal streamer tubes, which are parallel to the horizontal ones, have been inserted in the X–Z view tracking. Furthermore, new tracking algorithms have been implemented in other views. The Y–Z view tracking (lateral tracking) was based on the hits of the East and West lateral streamer tubes (perpendicular to the horizontal ones) and on a combination of horizontal tube and strip hits. At least 5 hit clusters were required: 3 have to be on the lateral planes, the other 2 were either lateral clusters, horizontal clusters, or both. This tracking algorithm enlarged the acceptance in the zenith region with $|\cos\theta| < 0.2$ by a factor ~ 1.4. In Fig. 19 an event is shown in which the lateral tracking permitted us to recover the attico hits belonging to the track. The first two plots are referred to X–Z and D–Z views, the last one to the Y–Z view. The track is properly reconstructed in each view.

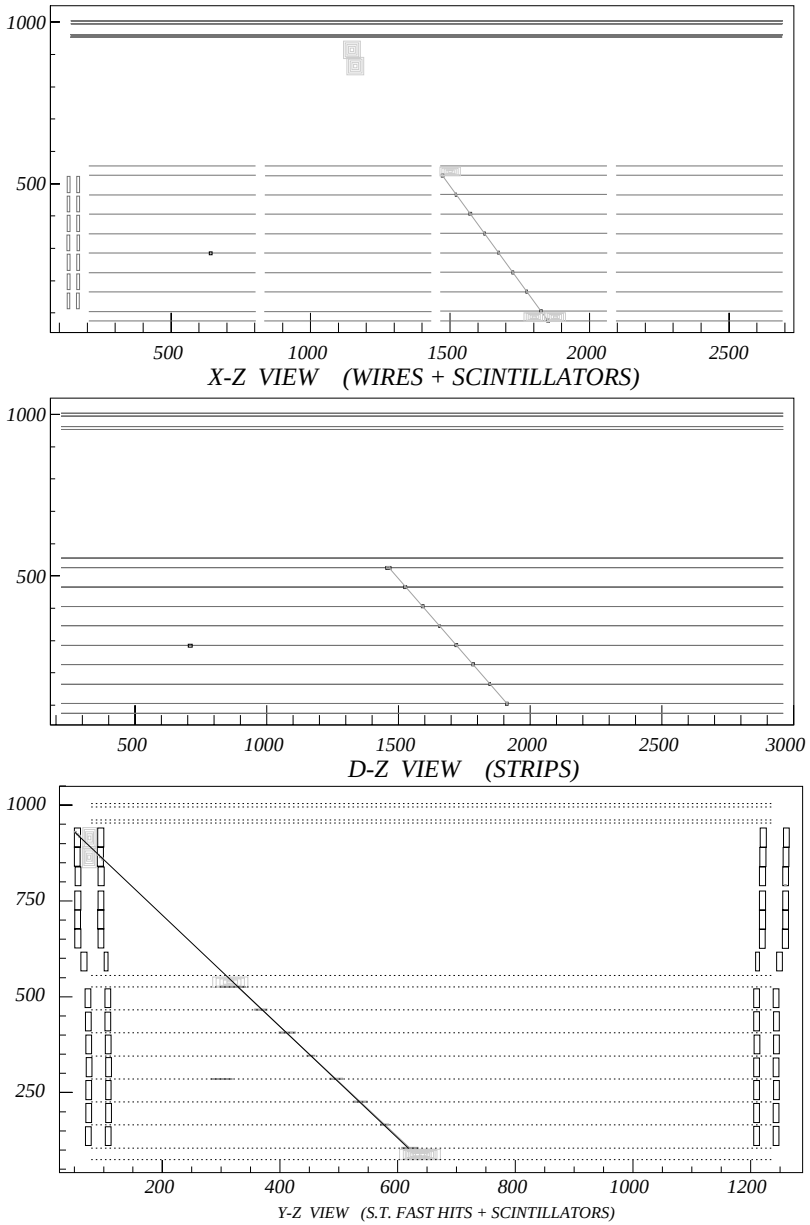

Fig. 19. Display of a neutrino-induced event (upward-going muon). The track is reconstructed by means of the horizontal streamer planes (the "X–Z View" for the wires and scintillators, and the "D–Z View" for the strips) and of the vertical streamer planes (the "Y–Z View"). In this event the central tracks are reconstructed only in the lower part of the apparatus. The lateral track recovers also lateral streamer hits in the attico. The boxes represent the scintillator hits.

The X–Y view tracking (attico strips) was based on the attico lateral pick-up strips. Because of the geometry of the apparatus, this algorithm was similar to the one used for lateral tracking. This X–Y tracking almost doubled the acceptance for muons with $|\cos\theta| < 0.2$.

The reconstruction of the track in space was mainly based on central track matching. Wire and

strip tracks in the horizontal plane views were associated by geometrical criteria (containment of associated hits in the detector active volume) and by comparison of the hit plane pattern. Also attico strip and lateral tracks could be matched to one another and to the central tracks. In this case the matching was based on the identification of a common subset of horizontal plane hits.

When only a Y–Z track resulted from the initial reconstruction, a spatial reconstruction was still sometimes possible. We were able to produce a space track when there were at least three pairs of horizontal tube and strip hits belonging to the track, but not otherwise. Typically, when there were more than three such tube-strip hit pairs, the initial reconstruction successfully generated a full space track.

When tracks in different views could be associated, we were able to improve the quality of track reconstruction by using a chi-squared minimization procedure. An example of associated tracks was shown in Fig. 19. This procedure is highly efficient for low multiplicity events (no more than 3 muons). For high multiplicity events, a different technique was used [35].

4.5.2. Geometry survey and tracking correction

The geometry of MACRO was precisely surveyed by standard methods and the positions of streamer tubes and strips were checked by muon tracking. Minor correction were introduced (less than 0.5 cm for horizontal planes, up to some centimeters for lateral planes). Finally muon tracking in the streamer tubes permitted a cross check of the scintillator geometry.

4.5.3. Tracking angular resolution and absolute pointing

One of the most important characteristics of the MACRO detector was its excellent angular resolution combined with its large acceptance. Consequently the experiment was sensitive to very faint cosmic point sources which could produce underground muons. It was, therefore, important to fully understand the detector's actual angular resolution for through going cosmic ray muons. This angular resolution was dominated by multiple Coulomb scattering in the rock overburden but it also included small components from the spatial resolution of the STs and the average error in their track reconstruction.

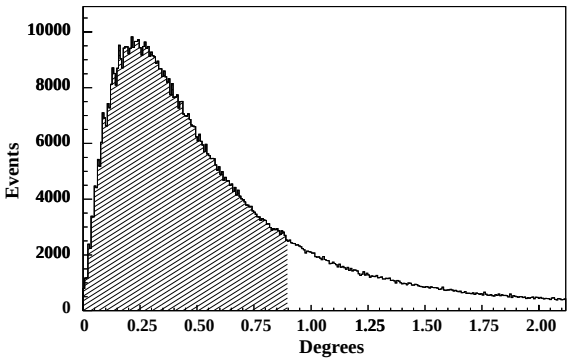

Fig. 20. Space angle distribution for double muons. The shaded area, covering angles less than 0.9°, contains 68.3% of the total area.

The space angle between double muons, as shown in Fig. 20, was used to infer the overall angular resolution of the apparatus. The data shown were taken after the attico was installed and it shows that 68.3% of the events have a space angle $\theta \leqslant 0.9^\circ$ between the two muons. If we assume that each muon was scattered independently, then the overall scattering angle for a single muon is $0.9^\circ/\sqrt{2} \simeq 0.64^\circ$, better than our previous published value of $1.3^\circ/\sqrt{2} \simeq 1.0^\circ$ [10].

Using the well known shadow in the cosmic rays of the moon [36–39], we independently estimated the actual angular resolution of the apparatus. By observing this shadow (see Fig. 21), we also verified the absolute pointing accuracy of the apparatus. MACRO's observation of the moon's shadow was the first such detection underground, and its analysis is detailed in a separate publication [40], in which it is shown that the angular resolution found in this way is in agreement with what is obtained using double muons.

4.5.4. Timing performances and charge measurements

The timing capabilities and charge sensitivity of the ST system and of the related electronics have played a central role in the ability to search for magnetic monopoles in the $10^{-4} \leqslant \beta \leqslant 5 \times 10^{-3}$ velocity range.

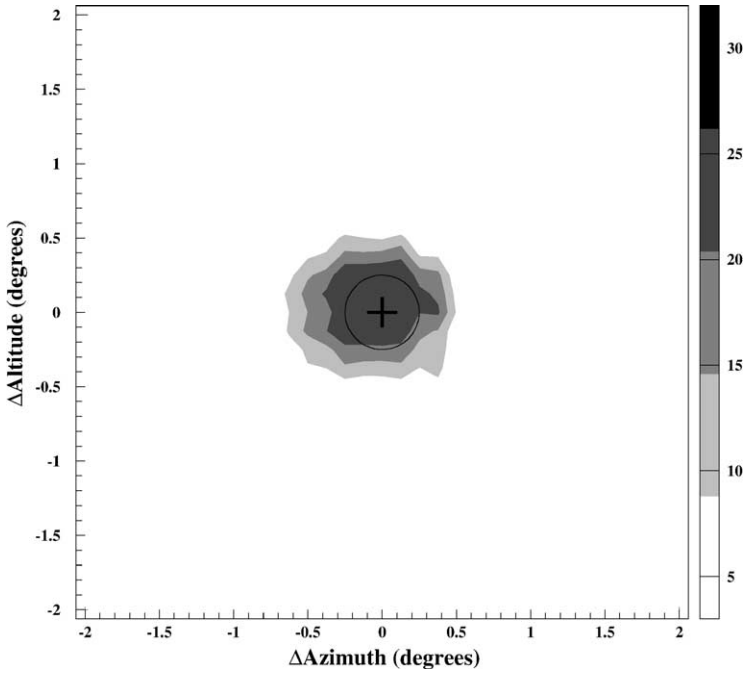

Fig. 21. Shadow of the moon measured as χ^2 levels (scale at right). The superimposed disk corresponds to the moon in its expected position without taking the geomagnetic displacement into account. The region centered on the moon position has a $\chi^2 = 32$ corresponding to a signal of statistical significance of about 5.6 σ.

Charge and time of the streamer pulses were recorded by the QTP system fully described in I and [41]; here we give only a brief discussion of the overall system performance extracted from the study of single muon events.

Time information from the QTPs was used to search for a time alignment of hits from different detector planes (time track). Time track parameters were used to compute the time of flight of particles in the lower part of MACRO. Fig. 22 shows the distribution obtained for a sample of $\sim 7 \times 10^5$ muons as reconstructed by the analysis used in the search for magnetic monopoles in the streamer tube system. The distribution is nicely Gaussian with a mean value of ~ 15 ns corresponding to the flight time of relativistic particles through the ~ 4.8 m height of the lower MACRO. Its standard deviation is ~ 120 ns, fully compatible with the expectations due to the drift time jitter of ionization electrons in the tubes. This resolution allowed us to effectively search for slowly moving monopoles ($\beta \leqslant 5 \times 10^{-3}$), rejecting relativistic particles by a time of flight cut.

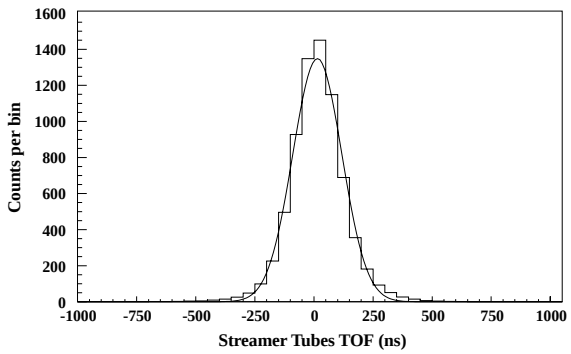

Fig. 22. ST measurement of time of flight of muons crossing lower MACRO.

The logarithmic response of the streamer charge to high ionization is used to search for faster monopoles [31]. Although the energy loss (Q_M)of $\beta \geqslant 5 \times 10^{-3}$ monopoles exceeds $\sim 10^2$ times that (Q_μ) of relativistic muons, the logarithmic dependence of the streamer charge to ionization, and the response of the front end electronics compress the minimum Q_M/Q_μ ratio to ~ 4. As a consequence,

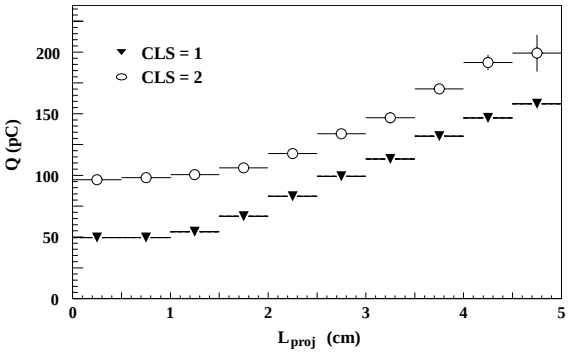

Fig. 23. Dependence of the streamer charge on the projected length of the track along the wire for tracks firing 1 tube (CLS = 1) and two adjacent tubes (CLS = 2).

we made careful corrections to the measured streamer charge accounting for geometrical effects [32] and small, long term variations in the gas composition. As an example, the streamer charge measured for single muons as a function of the track projection along the wire direction is shown in Fig. 23 for tracks firing one and two adjacent tubes in one plane, respectively.

4.5.5. Streamer tube sensitivity

Over its lifetime, the ST system detected cosmic ray muons with uniform efficiency. This was demonstrated by examining its sensitivity to very small variations (at the percent level) in the absolute muon rate over a long period of time. In particular, the seasonal variations of the underground muon flux were studied.

Data collected with all 6 lower SMs from 1991 to 1997 were used to search for seasonal variations in the observed muon rate. These rate variations are due to the density variations in the upper atmosphere caused by seasonal temperature changes. Density variations in the interaction region for primary cosmic rays affect the underground muon rate by changing the ratio of nuclear interaction to decay of secondary pions and kaons in the induced air showers. A complete description of this analysis is given in Ref. [16].

The data were analyzed by using the expression:

$$\frac{\Delta R_\mu}{\overline{R_\mu}} = \alpha_T \frac{\Delta T_{eff}}{\overline{T_{eff}}} \tag{11}$$

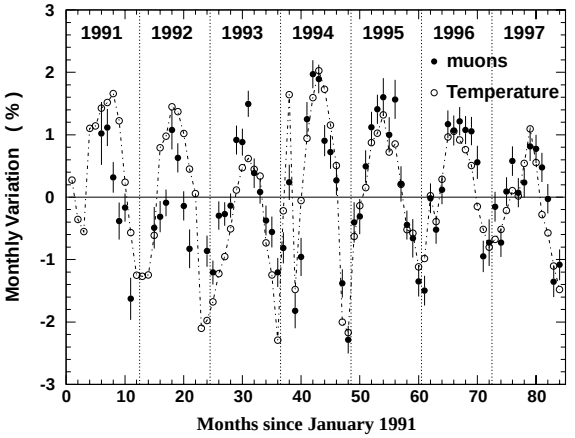

Fig. 24. The superposition of the percentage fluctuations in the muon rate, $\Delta R_\mu/\overline{R_\mu}$, and the percentage fluctuations of the effective temperature, $\Delta T_{eff}/\overline{T_{eff}}$, since January 1991.

where R_μ is the muon rate, α_T is the temperature coefficient, and T_{eff} is the effective temperature, defined as a weighted average of temperatures measured at different isobaric levels. It is given by

$$T_{eff} = \frac{\sum_i T(x_i)\exp(-x_i/\lambda)}{\sum_i \exp(-x_i/\lambda)} \tag{12}$$

where λ is the effective mean free path for nuclear interactions of secondary pions and kaons and x_i is the atmospheric depth at the ith isobaric level.

The expected size of this effect is $\alpha_T = 0.96$ [42], and although this implies that the rate fluctuations are at the percent level, we nevertheless measured them and determined the temperature coefficient to be 0.83 ± 0.13. In Fig. 24, the observed relative rate variations are superimposed on the observed relative temperature variations. The maximum variations from the mean are seen to be of order of $\pm 1\%$, and the excellent correlation is clear.

5. The nuclear track detector

The main purpose of the nuclear track-etch detector was to perform combined and independent searches for magnetic monopoles and other rare massive particles (i.e. nuclearites). It was placed horizontally in the middle of the lower detector, and vertically on the east (lower and

upper) and north (lower) walls. It was organized in stacks (“wagons”), consisting of three layers of CR39, each 1.4 mm thick, three layers of Lexan, each 0.2 mm thick, and an aluminum absorber 1 mm thick. Each wagon was placed in an aluminized Mylar bag filled with dry air and each could be inserted or removed by sliding it over rails.

The effective surface of the horizontal detector was 812 m^2 (13536 “wagons”, $24.5 \times 24.5\ cm^2$ each). On the north vertical surface there were 816 wagons of $24 \times 24\ cm^2$ area, corresponding to 47 m^2. On the east wall there were 7008 wagons, corresponding to 404 m^2. The total nuclear track detector surface was thus 1263 m^2; its total acceptance was 7100 m^2 sr for an isotropic flux of fast magnetic monopoles.

5.1. The CR39 nuclear track detector

The track-etch subdetector used two types of nuclear track detectors, CR39 and Lexan. Most of the work concerned the development and processing of CR39. Lexan has a much higher threshold compared to that of CR39, making it sensitive only to relativistic monopoles. Since no magnetic monopole candidates were found in the CR39, there was no need to analyze any of the Lexan in this experiment.

The CR39 was made by the Intercast Europe Co. (Parma, Italy) in several batches from 1988 to 1999. Calibrations were made using both relativistic and low velocity ions, and they covered a range from about 25 MeV $cm^2\ g^{-1}$ to about 6×10^3 MeV $cm^2\ g^{-1}$ in Restricted Energy Loss (REL, the energy loss within a 10 nm cylinder around the particle’s trajectory) and from 4×10^{-3} to ~ 1 in $\beta = v/c$.

5.1.1. Calibrations with relativistic ions

The CR39 batches were calibrated at different times with several species of relativistic heavy ions: (i) oxygen nuclei of 16 GeV $nucleon^{-1}$ at the BNL-AGS (1988), (ii) neon nuclei of 585 MeV $nucleon^{-1}$ at Berkeley (1990), (iii) silicon nuclei of 14.5 GeV $nucleon^{-1}$ at the BNL-AGS (1990), (iv) sulfur nuclei of 200 GeV $nucleon^{-1}$ at the CERN-SPS (1990), (v) gold nuclei of 11.3 GeV $nucleon^{-1}$ at the BNL-AGS (1992), (vi) lead nuclei of 158 GeV $nucleon^{-1}$ at the CERN-SPS (1994, 1996), and (vii) in 1999, iron nuclei of 1 GeV $nucleon^{-1}$ at the BNL-AGS [20,43–46]. Here we present the most recent calibration results obtained with the lead and iron beams.

Stacks of CR39 sheets placed before and after a target were exposed to 158 GeV $nucleon^{-1}$ Pb^{82+} and to 1 GeV $nucleon^{-1}$ Fe^{26+} ion beams. Each stack was composed of CR39 foils from different batches; it was then possible to determine the response of each batch to the same incident ion. The exposures were carried out at normal incidence at a density of ~ 400 ions cm^{-2}. When passing through the stack, the incident ions produced nuclear fragments with $Z < 82$ and $Z < 26$ for the lead and iron beam, respectively. Both the beam and the fragment ions with electric charges above the detector threshold were recorded.

After exposure to the lead (iron) ions the CR39 foils were etched in a 6-normal NaOH water solution at 70°C for 30 (45) h. Conical etch-pits are formed on each side of a detector foil along the ion path. The etch-pit base areas, their eccentricity, and central brightness were measured with an automatic image analyzer [47], which also provided the absolute coordinates of the etched cones; this allowed the tracking of the detected nuclei through the stack.

A typical average base area distribution is shown in Fig. 25. It refers to the CR39 made in November 1995 and etched for 30 h in 6-normal NaOH at 70°C shortly after exposure to the lead beam. The averages are made over six measurements of the bases of the etched cones in three CR39 foils. A large number of peaks is evident. Each peak corresponds to a relativistic nuclear fragment with different charge. The lowest detected charge is $Z = 5$.

The response of the CR39 is measured by the reduced etch ratio $p = v_T/v_B$, where v_T and v_B are the etching rates along the particle track and of the bulk material, respectively. For each detected ion, p was calculated based on the measurements of the surface areas of the etch-pits and of the bulk etching rate v_B.

In Fig. 26 are shown the calibration points, p versus REL for the CR39 foils, produced from

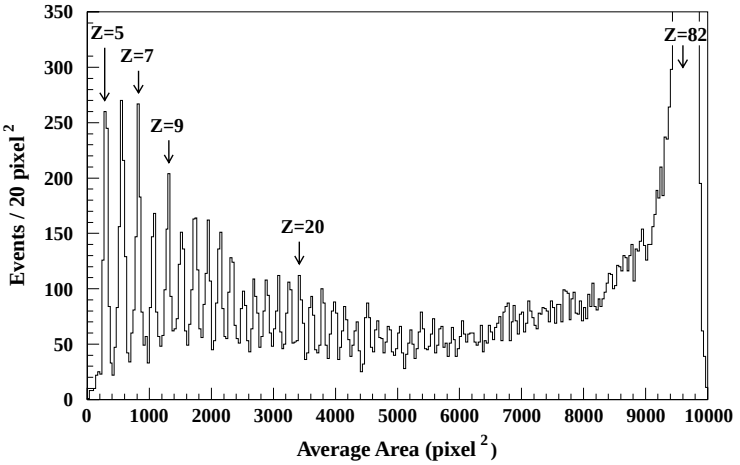

Fig. 25. Number of nuclear fragments from the fragmentation of relativistic Pb ($Z = 82$) ions in aluminum; the horizontal scale is the average etch-pit base area, which is proportional to the charge Z of the nuclear fragment.

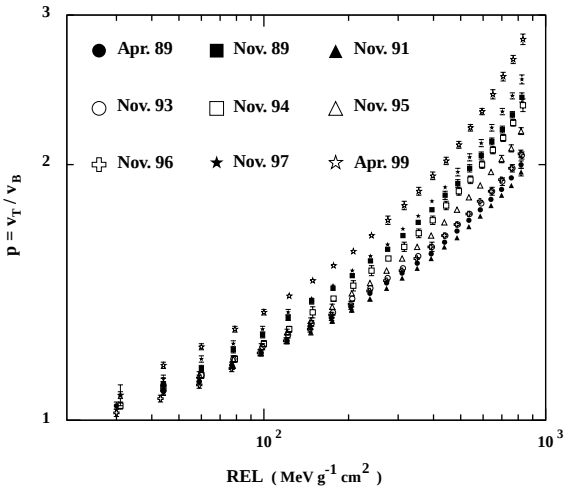

Fig. 26. Calibrations of CR39 of different production batches exposed to the 1 GeV/nucleon iron beam (BNL-AGS, 1999).

1989 to 1999, and exposed to the BNL-AGS Fe^{26+} beam of 1 GeV nucleon^{-1}. In general we can say that each production batch has its own calibration curve with no evident connection with the production time. The variations are mainly due to slightly different production conditions.

By comparing the results from different exposures we were able to test the existence of possible aging and fading effects of the MACRO CR39. Details are given in Ref. [46]; within experimental errors, no aging or fading effects were observed.

5.1.2. Calibrations with slow ions

Samples of CR39 were exposed to protons and deuterons from 50 to 200 keV and to beryllium and silicon ions from 100 to 400 keV [44]. Other samples were irradiated with $^4He^{2+}$ nuclei of 6 and 10 MeV. After exposure, the samples were etched in 6-normal NaOH water solution at 40.0°C for different times, ranging from 1 to 14 h. In Fig. 27 the measured p-values are plotted versus REL.

The solid circles correspond to relativistic nuclear fragments with charge $8 \leqslant Z \leqslant 68$ and the other points are for other nuclei and energies as indicated. The reduced etch rate for low velocity ions follows the relativistic calibration curve. These results show that the response of the CR39 used in this experiment is well described by a single curve of the reduced etch rate, p, versus REL both for relativistic ($\beta \sim 1$) and for low velocity ions, down to $\beta = 4 \times 10^{-3}$. Furthermore, within the limits of the available statistics and of the systematic uncertainties, our results are compatible with a full contribution of the nuclear stopping power to the CR39 response.

5.2. Search for magnetic monopoles with the track-etch detector

The restricted energy losses of magnetic monopoles of different magnetic charges in the nuclear

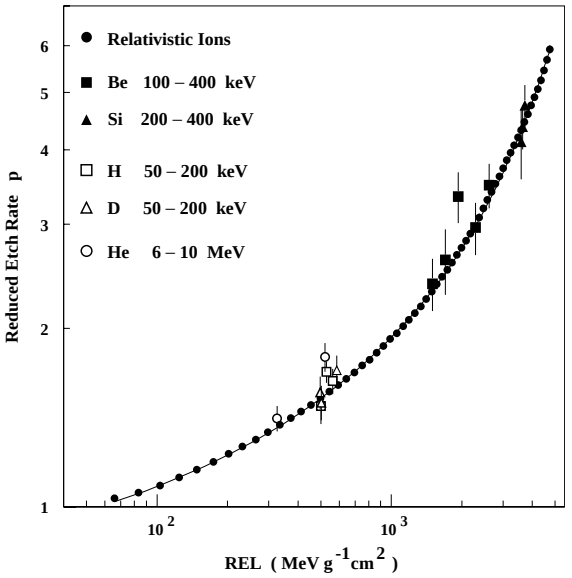

Fig. 27. Measured values of the reduced etch rate p versus REL for high velocity and low velocity ions; the solid line is the best fit through the relativistic data points (solid circles).

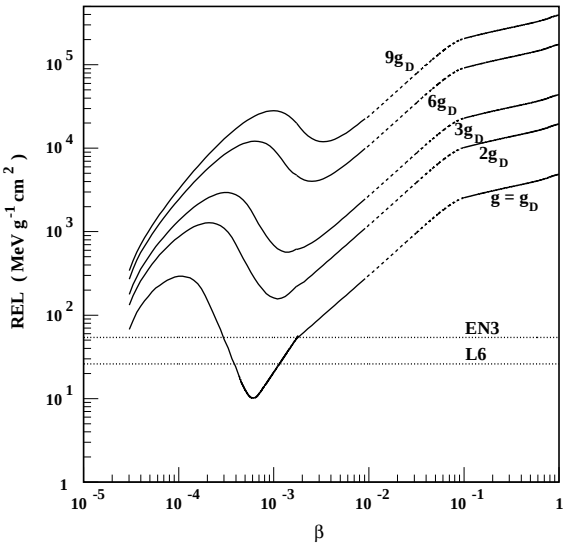

Fig. 28. Restricted Energy Losses versus β for magnetic monopoles with magnetic charge $g = g_D$, $2g_D$, $3g_D$, $6g_D$ and $9g_D$. in the CR39 nuclear track detector. The detection thresholds of two types of CR39 used by the MACRO experiment (EN3 and L6) are also shown.

track detector CR39 are presented in Fig. 28 as a function of β.

The detection thresholds of two types of CR39 used by the MACRO experiment (EN3 and L6) [48] are also shown.

The track-etch detector was used both as a stand-alone detector and in a "triggered mode" with the scintillator and ST systems.

Until now 530 m^2 of nuclear track detector have been etched and analyzed; the analysis was limited to the CR39 sub-detector only. In May 2000 we began the analysis of the entire nuclear track detector, which we plan to complete by April 2002.

5.2.1. Etching and analysis of CR39

After extraction from the apparatus, three fiducial holes of 2 mm diameter are drilled in each "wagon" with a precision drilling machine (the position of the holes is defined to within 100 μm accuracy). The top CR39 foils (labeled "L1") are "strongly" etched in a steel thermostatic tank (24 foils/etching tank) in a 8-normal NaOH water solution at 80–90°C until their final thickness is about 300–400 μm. An estimate of the bulk etching rate is obtained by measuring the initial and final thickness of four foils. After a "strong" etching the surface of the sheet is opaline. The signal we are looking for is a hole or a biconical track with the two base-cone areas equal within the experimental uncertainties. In order to test the existence of possible frontside–backside systematic differences, several stacks from the MACRO detector were exposed in December 1999 to the BNL-AGS iron beam, at 0°, 30°, and 45° incident angles. Strong etching was performed on the L1 foils and, for each incident angle, the minor axes on the front (a_F) and back side (a_B) of each sheet were measured for about 100 tracks. We obtained $a_F/a_B = 1.00 \pm 0.02$ (3 standard deviations) for all angles, showing the good front–back uniformity of the detector response.

Once etched the sheets were scanned twice by different operators with a $3\times$ magnification optical lens looking for any possible optical inhomogeneity. An optical inhomogeneity is usually a particle track or a defect of the material. The double scan guaranteed an efficiency of 100% for finding a possible signal. The detected inhomogeneities were then observed with a stereo $40\times$ microscope. About 10% of them were classified as

"tracks" and required further analysis. Each track was observed under an optical microscope with 80× or 160× magnification; the minor axes in the front (a_F) and the back (a_B) sides were measured. We required that $D = |a_F/a_B - 1| \leqslant 3$ times the error on the difference; this condition was satisfied by about 20% of the tracks.

In order to compute the p-values and incident angles θ for the front and back sides, the track major axes were measured too. Finally a track was defined as a "candidate" if p and θ on the front and back sides were equal within 15%. For each candidate a coincidence in positions, angles and RELs was required in the corresponding CR39 bottom layer (labeled L5) and, if necessary, also in the intermediate layer (labeled L3).

The L5 layers were etched in 6-normal NaOH water solution at 70°C. Thickness measurements were made to determine the bulk etching rate v_B (~ 1.2 μm h^{-1}). Using the measured incident direction of a "candidate" with its uncertainty and the fiducial marks, we selected an area of about 0.5–1 cm^2 in the L5 layer. This area was accurately scanned under an optical microscope with high magnification. The number of analyzed L5s was 5–10% of L1 layers. If a two-fold coincidence had been detected, the CR39 L3 layer would also have been analyzed in the same way as L5. However, up to now, no two-fold coincidence has been found, that is, no magnetic monopole, nuclearite or charged Q-ball candidate has been detected.

The 90% C.L. upper limits on the $g = g_D$ monopole flux from this measurement is at the level of 2.4×10^{-16} cm^{-2} s^{-1} sr^{-1} at $\beta \sim 1$, and 3.5×10^{-16} cm^{-2} s^{-1} sr^{-1} at $\beta \sim 10^{-4}$.

6. The TRD system

Transition radiation detectors are commonly used for fast particle identification both in the new generation accelerator experiments [49] and in cosmic ray physics [50,51]. Transition radiation (TR) is emitted in the X-ray region whenever an ultrarelativistic particle crosses the interface between two materials with different dielectric properties. Since this radiation increases (over a certain range) as a known function of the incident particle's Lorentz factor γ, it is possible to evaluate a particle's energy $E = m\gamma c^2$ in this range if the mass m is known.

For MACRO we built three TRD modules with 36 m^2 total surface area (see Fig. 29). In the Gran Sasso laboratory, the distribution of the muon residual energy is estimated to be nearly flat up to 0.1 TeV and to fall rapidly in the TeV region; its mean value is ~ 0.31 TeV. Thus, the TRD was designed to be sensitive in just this muon energy

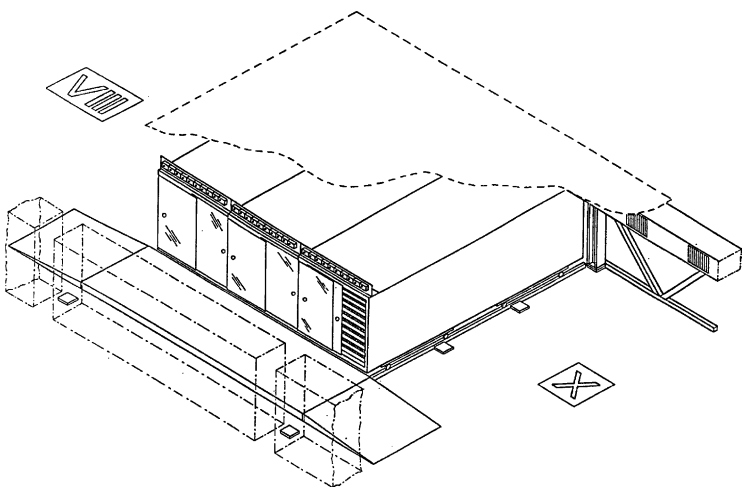

Fig. 29. Artist's view of the three TRD modules mounted on rails on the top of MACRO. The electronics racks, positioned 2 m from the front of the detectors, are also shown.

range, from 0.1 to 1 TeV. Below this range there is no transition radiation and the detector exhibits a smoothly increasing response versus γ resulting from the relativistic rise of the muon ionization energy loss in the TRDs gas-filled counters. For energies greater than 1 TeV, where the ordinary muon flux is estimated to be about 6% of the total, the transition radiation signal is saturated.

The measurement of the energy of muons in the TeV region, even with modest resolution, opens a wider range of experimental opportunities for cosmic ray physics both in underground and in surface laboratories. In fact, this technique allows direct measurement of the muon energy spectra in an underground experiment, independent of both assumptions about zenith angle distribution and the calculations of the energy loss in the surrounding rock that are usually needed [52].

6.1. TRD general description

A typical TRD consists of an array of radiators and proportional chamber layers. In our case, the chamber consisted of independent 6 m long proportional counters, each with a $6 \times 6\ \mathrm{cm}^2$ square cross-section and 0.9 mm thick polystyrene walls. These counters were positioned close together between radiator layers thereby reducing inefficient zones [53].

The readout of the TRD was based on the "cluster counting method". In this method, the wire signal is sharply differentiated in order to discriminate the ionization clusters produced by X-ray photoelectrons from the δ-ray background. Requiring a minimum number of counts in a cluster discriminated fast radiating particles from slower non-radiating ones.

Each of the three TRD modules had an active volume of $6 \times 1.92 \times 1.7\ \mathrm{m}^3$ and was based on 10 layers of 32 tubes each, interleaved by 10 foam radiator layers 10 cm thick. This radiator material was made of polyethylene foam. We selected Ethafoam 220 (about $35\ \mathrm{g\,l}^{-1}$ density) that exhibits cells of approximately 0.9 mm diameter and 35 μm wall thickness. This ensured a relatively wide range for the measurement of γ, corresponding to the desired energy region for muons. The bottom tube layer was placed on an eleventh radiator. Thus the detector was symmetric with respect to upgoing and downgoing muons, and so it could measure the energy of upgoing neutrino-induced muons that passed through it.

The counter cross-section, $6 \times 6\ \mathrm{cm}^2$, was a compromise between efficiently converting the transition radiation photons in an argon-based gas mixture and, at the same time, keeping a muon's ionization energy release at a relatively low level. The counters were built from extruded tubes internally painted with graphite to a resistivity of $10\ \mathrm{k\Omega\ square}^{-1}$. They were filled with an Ar (90%)–CO_2 (10%) mixture for safety and low cost. With this gas mixture and a 2540 V high voltage supply, the gain was maintained at about 10^4, providing good proportionality for photons up to 22 keV energy.

We measured the uniformity of the signal pulse height along and across the anode wires with a collimated ^{55}Fe source and found that it was uniform within $\pm 1.5\%$.

Searching for tracks in the TRD was done by using tracks reconstructed in the ST system. Hits in TRD tubes were assigned to an ST track when they were within ± 6 cm of it in the view perpendicular to the TRD anode wires. This assumption fully takes into account the localization uncertainty due to the finite resolution of the STs and at the same time it eliminates most of the spurious hits.

6.2. TRD readout and trigger electronics

The electronics readout for each counter wire is shown in Ref. [53]. It consisted of an analog section and a digital section mounted on a $5 \times 5\ \mathrm{cm}^2$ electronics card inserted in the tube endcap immediately after a 1 nF high voltage capacitor. The input stage of the analog section was a common base transistor which collected the wire current signal through a series resistor of 270 Ω, the characteristic impedance of the proportional tube. The output voltage pulse was shaped by a passive filter to a FWHM of about 80 ns and amplified using an NE 592 amplifier. The voltage gain of this stage was adjusted to about 100 by means of a variable resistor. The amplified pulse was sent through a buffer (LH0002) on an 8 m

long coaxial cable to the digital section. The dynamic range and the bandwidth of this section were 1 V and 20 MHz respectively, linear to within 1%. The typical pulse height produced by a 5.9 keV X-ray source on the 50 Ω termination at the digital section input was about 100 mV.

The digital section consisted of a fast comparator (LeCroy MVL 407 with an active delay of 450 ns to account for the signal readout trigger delay), a 3-bit counter (1/2 LS 393), and a shift register (LS 165). This section is housed inside a 32 channel standard NIM module (the "DISCAL" module) that processes one TRD tube plane. In order to discriminate clusters predominantly caused by transition radiation from δ-rays, the comparator threshold was set to 80 mV. This corresponded to about 5 keV energy, where the transition radiation spectrum starts. Signals above this threshold within a 1.4 ms time gate were counted and transferred in the shift register chain. In addition, the OR of these signals (DIGOR OUT) was available on the DISCAL module's front panel for monitoring and self-triggering purposes. The minimum signal width accepted by this stage was measured to be 12 ns, while the double pulse resolution was slightly higher.

The same STAS module used by the lower detector ST system, the CAEN C187, controlled both the bit transfer and the acquisition procedure by addressing each non-zero bit pattern. This module is able to process eight shift register chains, each with 1024 bits maximum length. For a TRD module readout corresponding to 320 channels of 3 bits each, only a single STAS chain was needed. For each event five words were read out in an average time of 10 ms.

The TRD trigger was based on standard NIM logic modules. The 10 DIGOR signals from the 10 proportional tube layers for each TRD module opened a corresponding acquisition gate. This operation allowed the tube hits to be stored in scalers used as memory buffers. They were read out whenever a muon trigger occurred within 10 ms. The observed rate of events crossing all ten TRD planes was about 120 muons per day per TRD module. Since natural radioactivity produced a counting rate of about 1000 Hz per TRD module, the probability for an accidental coincidence was 10^{-2}, corresponding to one accidental per day on the average.

6.3. Performance of the TRD

To investigate the γ dependence of the response of a TRD suitable for MACRO use, we set up a test beam at the CERN-SPS with a maximum momentum of 5 GeV c^{-1}. It consisted of two threshold Cherenkov counters to distinguish electrons from pions, and a 10 radiation-length lead-glass counter to select electrons. At 5 GeV, we obtained a pion contamination of 10^{-4} in the electron beam. We built a prototype TRD of limited size in order to fit the available space in a test beam area. In this set of measurements we adopted the cluster counting electronic readout as described in Section 6.1 above.

The cluster count distributions for each setting could be easily fit by Poisson distributions with means of, at most, about 10 counts.

In Fig. 30 the mean number of clusters for Ethafoam are shown for various values of γ and beam crossing angles. The mean number of clusters obtained with electrons without radiators are shown only for 0° to demonstrate the relativistic rise and the Fermi density effect plateau of the energy loss of a highly relativistic particle in a gas layer. We get similar behavior for the other

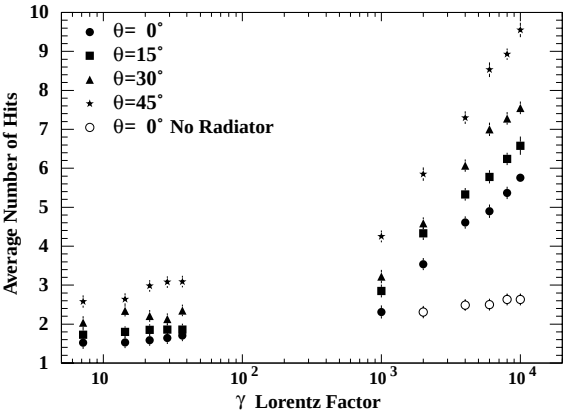

Fig. 30. Mean number of clusters for 10 cm Ethafoam radiator versus the Lorentz factor γ for various incident angles θ. The "no radiator" data show the relativistic rise and Fermi density effect of the ionization energy loss in the gas of the counters.

angle settings, namely a 10% increase in mean cluster number beyond $\gamma = 1000$.

7. The data acquisition system

In the first period of data taking, which ended in 1994, the detector was run with an acquisition system based on a network of MicroVAX-IIs and the CERN-Fisher CAMAC System Crate [54]. Subsequently, we upgraded the system in order to include VME front-end electronics, used particularly in the new WFDs for the scintillator counters. Such a system was described in some detail in Ref. [55]. The new system was based on a network (ETHERNET/DECNET) of KAV30 VAX processors and MicroVAX-IIs. The KAV30 is a VME single-board computer based on the rtVax 300 real-time processor. It includes a CVAX microprocessor, a floating point coprocessor, and a second generation Ethernet controller and it allows VAXELN applications to interface with VMEbus devices. VAXELN is a Digital Equipment software product specific for the development of dedicated, real-time systems for the VAX family of computers. The general layout of the new data acquisition system is shown in Fig. 31. Three KAV30 processors controlled three groups of two SMs, while three additional MicroVAX-IIs acted as the supervisors for the PHRASE trigger that looked for neutrino events originating in a stellar collapse. Each VME crate where a KAV30 processor was located acted as a VME Master Crate.

The VME Master Crate was able to drive several VME crates by means of the CES VIC8250 VMV master/slave interface on the VMV bus (Vertical Bus). In our system, the distances between master and slave crates was on the order of a few meters.

The VIC8250, a one-slot VME module, offers a transparent interconnection of up to 15 VME crates on the VMV bus, each crate being identified by a crate number. In such a VMV system, all VME busses are autonomous and completely independent. When the CPU located in the VME Master Crate accessed a slave device in a remote

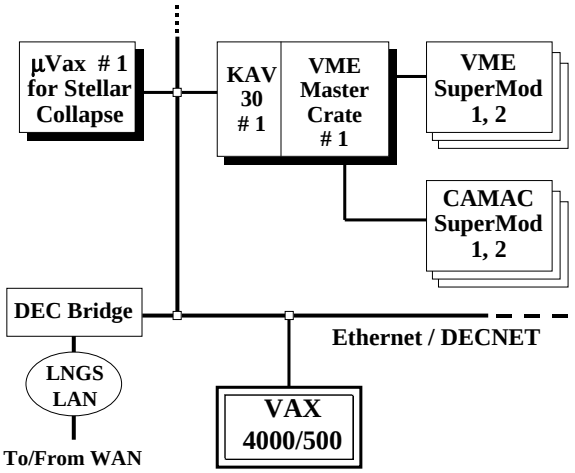

Fig. 31. General layout of the data acquisition system.

VME crate, the two were linked only during the cycle and were independent the rest of the time.

A remote device was accessed by mapping a 1 Mbyte page of the addressable memory space in the remote crate onto the VME Master Crate memory space. This was done by writing a longword, the *page descriptor*, into a specific location of the VIC8250 CSR space. The page descriptor contained the remote crate number, the VME address of the device in the remote crate, and the address modifier. For example, if we wanted the CPU to access the remote memory resource through the VME standard address XXX, the page descriptor had to be written in the CSR into an address which depended on address XXX. Thus the addressing of the remote physical memory, once mapped, was completely transparent to the user.

With the KAV30 processor, it took about 2.0 μs to write a word/longword on a VME Master Crate and about 2.1 μs for the same operation on a remote VME crate via VMV bus. The times for read operations were slightly longer.

CAMAC was accessed from VME by means of one or more CES CBD8210 (CAMAC Branch Driver) interfaces, each one controlling a full CAMAC Branch. The CBD8210 supported both 16-bit and 24-bit data transfer. CAMAC crates were accessed by mapping a CAMAC address field onto the 24-bit address field of VME. Two

Interrupt Request (IRQ) lines with front-panel external inputs were also provided. These IRQs were used in our system for event and alarm interrupts respectively. The extension board CES DMC8211 was also used for DMA block transfers to and from CAMAC crates. Two CAMAC parallel branches were connected to each VME Master Crate. Single word transfers from a CAMAC crate, using the KAV30 and CBD8210, required about 4.1 and 7.0 μs for 16-bit and 24-bit data respectively.

The tasks performed by each front-end processor were: electronics readout, event filtering (planned but not used), data reduction, apparatus monitoring, calibration, and data forwarding to a central VAX4000/500. This central computer, running under the VAX/VMS operating system, was used as a file and network server and as a user interface to the acquisition system. It also provided the disks for raw data logging. All the computers, including the VAX4000/500, were connected under the DECNET protocol via Ethernet as the MACRO Local Area Network (LAN) and this, in turn, was connected to the general LNGS LAN by a DEC Bridge. The VAX4000/500 was also connected to the general LNGS LAN under the TCP/IP protocol. The LNGS LAN was composed of segments linked via optical fibers running for about 6 km between the underground laboratory and the external laboratory where the general computing facilities were located. From the external laboratory there was access to the Wide Area Network (TCP/IP and DECNET at the beginning of data acquisition).

Utilities were implemented to help in controlling and debugging the apparatus. Thus, during data acquisition, a user at any DECNET node could request a copy of the raw data buffer from a given front-end processor or from the central VAX, and could require the execution of CAMAC operations by using Remote Procedure Calls. These capabilities were very important in maintaining the efficiency of the experiment.

7.1. Acquisition system performances

The main advantages of VAXELN relative to the VAX/VMS operating system have been summarized elsewhere [54]. Here we only want to point out that this software operated in a host and target system environment.

The VAXELN system for the experiment consisted of six user jobs running with different priorities, and four system jobs (the Ethernet driver, the console driver, etc.). In each job, many concurrent sub-processes could run with different priorities and, in our system, more than 15 sub-processes ran concurrently. In particular, each activated DECNET connection was handled by a dedicated sub-process.

All the software was written in EPASCAL, the PASCAL native language of VAXELN. The exchange of data between jobs was done using the VAXELN message facility which was very useful for handling queues of buffers.

The VME and CAMAC input/output during the data taking was done using a list of operations loaded from a file resident in the VAX4000/500. The basic element of the list was the *equipment*. This term denotes a logical block of VME and CAMAC operations, that is, a sequence of read, write, or test functions to be performed on electronics modules. Both single word operations and DMA transfer operations could be executed by inserting the proper instructions into the equipment definition. It was also possible to select a subset of operations inside any equipment by defining a *section* in the equipment. A set of equipment formed a *trigger*, that is, the full sequence of operations which were to be performed at the occurrence of a particular event trigger. The list also included an initialization part which contained the necessary operations (module resets, register zeroing, VIC VME mapping, etc.) executed at the beginning of a run.

CAMAC could also be accessed using a library of standard ESONE CAMAC routines and a set of fast VAXELN routines. This library (written in EPASCAL) was explicitly developed for the new system and it required the use of the CBD8210 VME board as interface between the VME Master Crate and the CAMAC branch. The CAMAC routines could be called either directly inside VAXELN or from a computer in the DECNET network using remote access routines.

Some I/O performances which we obtained using the list instructions in the acquisition task for VME and CAMAC access are reported in Table 1. In the same table, some I/O performances obtained using the ESONE CAMAC routine library are also given.

The performances obtained using the remote access CAMAC routines are listed in Table 2. In this case, performance was limited by the Ethernet throughput and by DECNET overhead. Of course, the throughput increases if many CAMAC I/Os are requested in the same call by the block transfer routine (CSGA) or by the DMA routine. This kind of access to CAMAC was very useful for debugging the electronics since it allowed writing and running simple programs on a VAX/VMS host requiring neither knowledge of VAXELN nor monitoring with slow devices.

Table 1
VME and CAMAC I/O performances in the acquisition task

Using the list	
VME word/longword transfer	
Single read in a remote memory	4.8 μs
CAMAC 16-bit data transfer	
Single operation (with Q test)	15.8 μs
Single operation (without Q test)	11.3 μs
Block transfer (without Q test)	4.6 μs
CAMAC 24-bit data transfer	
Single operation (with Q test)	21.9 μs
CAMAC DMA data transfer	
1st word	370 μs
Additional 16-bit words	3.0 μs
Additional 24-bit words	5.4 μs
Using the ESONE routines	
Single 16-bit data transfer (CSSA)	42 μs
Block 16-bit data transfer (CSGA)	
1st word	54 μs
Additional words	22 μs

Table 2
CAMAC I/O performances using remote calls from the VAX4000/500

Single CAMAC I/O using CSSA	5 ms
I/O of 10 CAMAC words using the ESONE list routine (CSGA)	7 ms
I/O of 10 CAMAC words using the ESONE DMA routine (CSUBC)	8 ms
I/O of 5000 CAMAC words using the ESONE DMA routine (CSUBC)	60 ms

At system saturation, the maximum global data throughput we obtained on the network, including the VAX4000/500, was about 130 kbytes s^{-1}.

In conclusion, the performance of our acquisition system was well suited to the needs of an experiment of the size of MACRO, particularly because of its modularity and its good hardware/software maintainability.

7.2. On-line monitoring

Several hardware and software systems were built for the on-line monitoring of the data acquisition of the experiment. The Event Display and the Diagnostic Monitor are presented in the following.

7.2.1. The event display

A specific software tool written for the on-line drawing of the detector data was the Event Display program (EVD). It is based on the ISO standard graphics package, GKS, and heavily uses GKS's picture segmentation characteristics, logical I/O device concepts, and metafile facilities.

The most important features available to the operators were:

- different 3D and 2D projection views of the events,
- the possibility of looking at different detector parts with different magnification,
- the possibility of selecting and displaying only particular event configurations,
- interactive tracking for streamer tubes hits.

The user interface of EVD was simple and intuitive: the program activities were seen as logically independent by the operator and were controlled by means of nested menu sequences. Event input data came from different sources: on-line data directly from front-end microVAX's, data previously stored on disk files, and network data. The raw data were encoded bytes which needed to be interpreted and processed according to the detector type. The event was accepted if it matched some requested selection criteria and the

picture was sent to the display surface after applying the transformation and view options previously chosen by the operator. The picture structure was built by creating several segments containing the output primitives which represented the current event data while a set of preselected segments defined the detector parts that had to be sent to the display (a portion of a module, one or more modules, etc.). Thus the large use of segmentation allowed us to satisfy the requirements of speed and interactivity. Moreover the event data spooling facility of VAX/VMS acquisition system tasks made it simple to monitor the on-line acquisition from the remote nodes of the network also.

7.2.2. The diagnostic monitor

With the aim of monitoring the DAQ operations to ensure continuous reliability of the data taking, an automatic DiaGNostic system (DGN) was built. It was able to collect data in parallel with the official data acquisition and data storage system but independently of it. Thus, it could quickly signal anomalous behavior in the apparatus. The digitized data provided by the acquisition electronics were collected event by event at the trigger rate, decoded, analyzed and grouped as statistical histograms, multidimensional maps, or functions of time. At the checking level, the current data were compared with a set showing the standard equipment status: differences produced a list of deviations and possible locations of the failures. At the same time the current status was condensed into a few graphs of prominent parameters to provide some display warnings to the operators.

From the hardware point of view, DGN was composed of several VME modules located in a dedicated crate. As stated above, the modules which digitized the detector signals were based on the CAMAC and VME standard. The VME interface in the DAQ Master crate mapped the addresses of the CAMAC registers containing the current data as VME addresses in a predefined memory space. So we provided a "spy" card, located in the Master crate, which identified the mapped addresses and latched the data present on the VMEbus during the event readout. These parasitic cards, one for each acquisition branch, transmitted the captured pairs of 32-bit address–data to memory cards located in the DGN crate. Each memory card contained 512 kbytes of RAM which, with suitable pointers, were handled as a circular buffer. An assembler program running on a 68020 CPU scanned the buffers and created pointers to sequences of relevant data; a second CPU in the crate, running under OS9, used these pointers to send the data blocks to the downstream software. The DGN crate hardware processor also contained VME cards to perform on-line tracking of the ST data. Several tasks ran concurrently on a DIGITAL 4000/90 dedicated workstation to perform the data checking and to provide the display interface. A task-to-task Ethernet link at an effective rate of about 0.2 Mbytes s^{-1} connected the VME CPU program to the workstation task which read, decoded, and stored the event data. A spy task performed the most significant part of the analysis event-by-event, while a display task graphically presented the data taking status (trigger rates, wire maps, muon rates, hit cluster distributions, etc.). Moreover a parallel task could operate as a remote display server, allowing the experiment to be controlled by people outside the tunnel. The DGN system could collect and analyze events at a rate up to 10 Hz. Data transfer was less than 50 ms $event^{-1}$ and the tasks on the VAXstation required about 60–80 ms to process an event.

7.3. The UTC clock

The timing of events relative to the international standard time scale was performed by the LNGS clock. This is synchronized with the Universal Time Coordinated, controlled by the United States Naval Observatory (UTC/USNO) standard via the Global Positioning System (GPS) time signals. As shown in Fig. 32, a *Master Clock*,[18] consisting of various components and located in the external laboratory, drives several peripheral units, called *Slave Clocks*, located near the LNGS underground experiments.

Each GPS satellite continuously broadcasts signals containing UTC/USNO time as well as

[18] ESAT S.r.l - Torino (Italy).

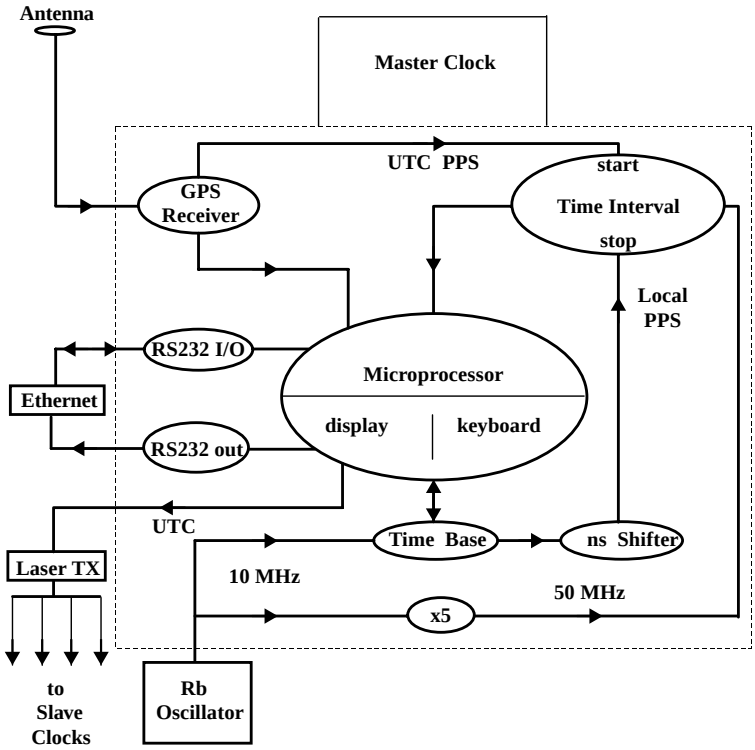

Fig. 32. Master Clock.

data on its trajectory, health and location. In order to calculate its own three-dimensional position, the GPS Receiver uses four channels to track the four satellites with the highest quality signals at any given time. After a sufficient number of position measurements are made to determine the receiver's position with an uncertainty of a few meters, it can be switched to a "time-only" mode, which then uses the predetermined precise position to convert the time messages received from the healthiest satellite to precise time pulses, PPS, synchronized with UTC/USNO.

Since the GPS Receiver unit itself is not directly accessible to the underground experiments for event timing purposes, a local time scale is generated by the Master Clock and is aligned to the UTC/USNO scale in the following way.

The GPS Receiver provides a time stamp message for each one-second roll-over signal, PPS, in the form of a serial string containing time, date and satellite status. This is used by a Microprocessor to generate the local time scale based on a 10 MHz frequency signal coming from a Rubidium Oscillator. This oscillator has high stability [56] with a fractional frequency long-term drift less than 10^{-11} month^{-1} and a short-term stability (Allan variance) of less than $3 \times 10^{-12}/100$ s.

Each second, the Time Interval unit (20 ns resolution) measures the time difference between the PPS signal from the UTC/USNO and the corresponding Local PPS signal from the local scale. Sixty of these time differences, corresponding to 1 min, are averaged to yield the quantity Δt whose distribution is shown in Fig. 33. The sources of these time drifts can be grouped in two classes:

- "short term" fluctuations, due to intrinsic noise on the time signal (transmitter, receiver, and signal propagation instabilities) and/or to the "Selective Availability", which is an artificial noise introduced by USNO in order to prevent civilian users from attaining the system's maximum position accuracy;

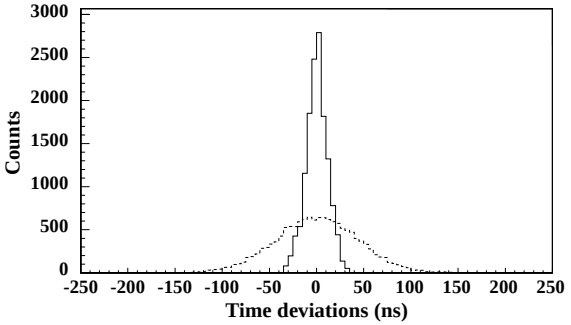

Fig. 33. The solid curve, with a mean of 0.33 ns and standard deviation of 11.5 ns, shows a typical distribution of time residual errors after all corrections have been applied. The dotted histogram, with a mean of 1.9 ns and standard deviation of 44 ns, is a typical example of the differences, Δt, between the UTC/USNO PPS signals and the Local PPS signals, averaged over 1 min.

- "long term" deviations due to frequency drifts of the local oscillator relative to UTC, coming from: (a) typical Rubidium Oscillator aging effects which can cause time drifts of the order of 1 μs per day, and (b) environmental conditions, mainly temperature variations, which become apparent within a few hours and cause deviations of the same order of magnitude as the ones discussed above.

The short term fluctuations, Δt, shown as the dotted curve in Fig. 33, normally did not exceed 100 ns, but we occasionally observed Δt values as big as few hundred nanoseconds, generally indicating non-optimal quality of the GPS signal.

Long term frequency drift can be detected by making a linear least squares fit of Δt to time itself. A slope significantly different from zero in this fit is an indication of long term drift in the local oscillator. It was shown that 180 measurements of the Δt values, corresponding to a time interval of 3 h, minimized the frequency deviations due to the combination of the two long term drift effects. The *time residual error* (the difference between local time and UTC time) was calculated each 60 s on the basis of the last 180 data points, and, when necessary, the *ns Shifter* made smooth corrections, properly shifting the local clock time scale by steps of 1 ns.

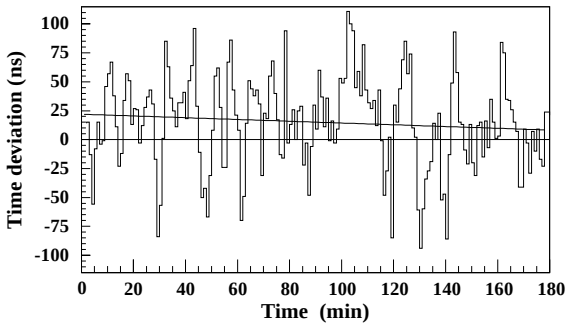

Fig. 34. The smooth curve shows the time residual error calculated every minute compared to the corresponding Δt values. The slope of the smooth curve in this sample is -4.9 ns/h.

In Fig. 34, the time residual errors, measured each 60 s resulting from the above procedure, are compared with the Δt of the short term fluctuations. Distributions of each are shown in Fig. 33. The typical ~ 12 ns standard deviation of the time residual error distribution is a measure of the magnitude of the instantaneous Master Clock time error.

This procedure provided excellent traceability of the local time scale to the UTC/USNO scale, which in turn was normally aligned within less than 100 ns to the international standard UTC scale.

7.3.1. Slave clocks

Each millisecond, the time/date information and a synchronization pulse were sent by the Master Clock through an 8 km long mono-modal 1310 nm wavelength optical fiber cable to a set of six Slave Clocks. Each Slave Clock corrected for the signal transit time and reproduced the UTC/USNO scale with a resolution of 0.1 μs. Event trigger signals coming from the different sections of the experimental apparatus latched these clocks and standard time and date (80 bits in total) were then recorded for each event.

8. Off-line data analysis

The offline analysis program Data Reduction and Event Analysis for MACRO (DREAM) is briefly described in I. It was used throughout the

life of the experiment as the primary off-line data analysis tool, having been continually upgraded both technically and functionally. Initially written on a VAX/VMS platform, it was subsequently ported to IBM/VM, IBM, DIGITAL, HP UNIX and Linux machines.

The data files produced by the acquisition system were transferred with a delay of ~ 1 day to a VAX/VMS computer in the external laboratory and immediately processed to produce DST files for neutrino and cosmic ray muon analyses. DST production for different analyses (for instance, monopole analysis) followed a different stream. Those files contain some raw quantities (ADC and TDC values) as well as reconstructed quantities as, for example, coordinates of the streamer tube hits, time and energy deposition of the scintillator counters, and parameters of the tracks in both detector systems.

DST files were written in VAX native mode. They contain only integer quantities and can be easily processed on different platforms. Reading of DST files can be performed by the same analysis program DREAM; in this way a reprocessing of the raw data (for example with different calibration constants) can be performed.

A procedure that ran on a dedicated ALPHA machine fully automated the production of DST files. All DSTs produced after the completion of the detector are stored on disk (total of 90 Mblocks = 46 Gbytes), while the older ones are stored on magnetic tapes. Both the procedure and the monitoring of the DST production were developed and maintained locally at the experiment site.

9. Conclusions

The MACRO detector was proposed in 1984; it was installed in Hall B of the underground Gran Sasso Lab in a modular way starting in October 1987. It started data taking in February 1989 with the first lower supermodule, and in 1995 with the complete detector. MACRO completed its program of data taking in December 2000.

During the data taking period the detector performed very reliably, and it did not have any major difficulty. The fraction of time the detector was on, the percentage lifetime, was very high and reached nearly 99% for the gravitational stellar collapse system.

During its lifetime, MACRO collected more than 60 million high energy downgoing muons, which allowed continuous checks of the apparatus as well as yielding interesting physics and astrophysics results.

MACRO obtained and published results on all the fields proposed and discussed in the 1984 proposal. Of particular relevance are:

- the new limits for GUT magnetic monopoles in the cosmic radiation,
- the results on atmospheric neutrinos and on their oscillations based on 3 event categories extending from a few GeV up to hundreds of GeV,
- the results on cosmic ray physics based on high energy downgoing muons and coincidences with the EASTOP detector located at Campo Imperatore.

Besides these results, many technical papers were published on the scintillator and streamer tube systems, on their monitoring, on the nuclear track and transition radiation detectors. Many analyses are still in progress including some new ones. Furthermore our analyses have stimulated great improvements in the Monte Carlo calculations dealing with high energy cosmic rays.

MACRO results have been published in 33 papers in international refereed scientific journals, in addition to many papers and invited talks at many international and national conferences. The scientific and technical results were used for a very large number of internal memos and for over 140 Ph.D. and undergraduate theses in Italy, US and Morocco (for a complete list available on the www, see Ref. [57]).

MACRO pioneered the new generation of large underground detectors for astroparticle physics and helped to develop the new Gran Sasso Lab.

Acknowledgements

We gratefully acknowledge the support of the directors and of the staff of the Laboratori

Nazionali del Gran Sasso and the invaluable assistance of the technical staff of the institutions participating in the experiment. We thank all our run coordinators. We thank the Istituto Nazionale di Fisica Nucleare (INFN), the US Department of Energy and the US National Science Foundation for their generous support of the MACRO experiment. We thank INFN, ICTP (Trieste), NATO and World Lab for providing fellowships and grants for non-Italian citizens.

References

[1] S. Ahlen, et al., Phys. Rev. Lett. 72 (1994) 608.
[2] M. Ambrosio, et al., Astropart. Phys. 6 (1997) 113.
[3] M. Ambrosio, et al., Phys. Lett. B 406 (1997) 249.
[4] M. Ambrosio, et al., Astropart. Phys. 4 (1995) 33.
[5] R. Liu, A search for fast moving magnetic monopoles with the MACRO detector, Caltech Dissertation, 1995.
[6] M. Ambrosio, et al., Phys. Lett. B 357 (1995) 481.
[7] M. Ambrosio, et al., Phys. Lett. B 434 (1998) 451.
[8] M. Ambrosio, et al., Phys. Lett. B 478 (2000) 5.
[9] F. Ronga, et al., Proc. XXV ICRC, Durban, South Africa, Vol. 7, p. 45;
M. Ambrosio, et al., Astrophys. J. 546 (2001) 1038.
[10] S. Ahlen, et al., Astrophys. J. 412 (1993) 301.
[11] S. Ahlen, et al., Phys. Lett. B 249 (1990) 149.
[12] M. Ambrosio, et al., Phys. Rev. D 60 (1999) 082002.
[13] S. Ahlen, et al., Astropart. Phys. 1 (1992) 11.
[14] M. Ambrosio, et al., Astropart. Phys. 8 (1998) 123.
[15] R. Bellotti, M. Aglietta, et al., Phys. Rev. D 42 (1990) 1396;
S. Ahlen, et al., Nucl. Phys. B 370 (1992) 432;
S. Ahlen, et al., Phys. Rev. D 46 (1992) 895;
S. Ahlen, et al., Phys. Rev. D 46 (1992) 4836;
M. Ambrosio, et al., Phys. Rev. D 50 (1994) 3046;
M. Aglietta, et al., Phys. Lett. B 337 (1994) 376;
M. Ambrosio, et al., Phys. Rev. D 52 (1995) 3793;
M. Ambrosio, et al., Phys. Rev. D 56 (1997) 1407;
M. Ambrosio, et al., Phys. Rev. D 56 (1997) 1418;
M. Ambrosio, et al., Phys. Rev. D 59 (1999) 012003;
M. Ambrosio, et al., Astropart. Phys. 10 (1999) 11;
M. Ambrosio, et al., Phys. Rev. D 60 (1999) 032001;
M. Ambrosio, et al., Astropart. Phys. 9 (1998) 105.
[16] M. Ambrosio, et al., Astropart. Phys. 7 (1997) 109.
[17] C.W. Walter, A search for lightly ionizing particles with the MACRO Detector, Caltech Dissertation, 1997.
[18] M. Ambrosio, et al., Phys. Rev. D 62 (2000) 052003.
[19] S. Ahlen, et al., Phys. Rev. Lett. 69 (1992) 1860;
M. Ambrosio, et al., Eur. Phys. J. C13 (2000) 453.
[20] S. Ahlen, et al., Nucl. Instr. and Meth. A 324 (1993) 337.
[21] C. De Marzo, et al., Nuovo Cimento 9C (1986) 281;
M. Calicchio, et al., Nucl. Instr. and Meth. Phys. Res. A 264 (1988) 18.
[22] G. Battistoni, Nucl. Instr. and Meth. A 279 (1989) 137.
[23] G. Battistoni, et al., Nucl. Instr. and Meth. 217 (1983) 429;
J. Allison, et al., Nucl. Instr. and Meth. 201 (1982) 341;
C. Becker, et al., Siegen University preprint SI-82-1, 1982.
[24] S.D. Drell, et al., Phys. Rev. Lett. 50 (1983) 644;
V. Patera, Phys. Lett. A 137 (1989) 259.
[25] M. Anelli, et al., Nucl. Instr. and Meth. A 289 (1990) 294.
[26] G. Battistoni, et al., Nucl. Instr. and Meth. 202 (1982) 459 and reference therein.
[27] G. Battistoni, Proceedings of the Second Workshop on Gas Sampling Calorimetry, Fermilab, 1986, p. 594.
[28] J. Reynoldson, Tesi di Laurea, Univ. dell'Aquila, June 1996.
[29] CAEN Technical Information Manuals for Models C267 and SY408.
[30] S.P. Ahlen, in: Magnetic Monopole, NATO ASI series, series B: phys., Vol. 2.
[31] G. Battistoni, et al., Nucl. Instr. and Meth. A 270 (1988) 185;
G. Battistoni, et al., Nucl. Instr. and Meth. A 401 (1997) 309.
[32] G. Battistoni, et al., Nucl. Instr. and Meth. A 399 (1997) 244.
[33] G. Auriemma, et al., Nucl. Instr. and Meth. A 263 (1988) 249.
[34] V.A. Rubakov, JETP Lett. 33 (1981) 644;
C.G. Callan Jr., Phys. Rev. D 26 (1982) 2058.
[35] M. Ambrosio, et al., Phys. Rev. D 56 (1997) 1407.
[36] G.W. Clark, Phys. Rev. 108 (1957) 450.
[37] D.E. Alexandreas, et al., Phys. Rev. D 43 (1991) 1735.
[38] M. Amenomori, et al., Phys. Rev. D 47 (1993) 2675.
[39] M. Aglietta, et al., Astropart. Phys. 3 (1995) 1.
[40] M. Ambrosio, et al., Phys. Rev. D 59 (1999) 012003.
[41] Nucl. Instr. and Meth. A 321 (1992) 609.
[42] P.H. Barrett, et al., Rev. Mod. Phys. 24 (1952) 133.
[43] R. Bellotti, et al., 21st ICRC, Adelaide, Vol. 10, 1990, p. 252;;
S. Ahlen, et al., Nucl. Tracks Radiat. Meas. 19 (1991) 641;
S. Cecchini, et al., Nucl. Tracks Radiat. Meas. 22 (1993) 555.
[44] S. Cecchini, et al., Nuovo Cimento 109A (1996) 1119.
[45] G. Giacomelli, et al., Nucl. Instr. and Meth. A 411 (1998) 41.
[46] S. Cecchini, et al., Proceedings of the 20th International Conference on Nuclear Tracks in Solids, Portoroz, Slovenia, August 2000.
[47] A. Noll, et al., Nucl. Tracks Radiat. Meas. 15 (1988) 265.
[48] J. Derkaoui, et al., Astropart. Phys. 10 (1999) 339.
[49] B. Dolgoshein, Nucl. Instr. and Meth. A 326 (1993) 434.
[50] K.K. Tang, Astrophys. J. 278 (1984) 881.
[51] E. Barbarito, et al., Nucl. Instr. and Meth. A 313 (1992) 295.
[52] L. Bergamasco, et al., Nuovo Cimento C6 (1983) 569.

[53] E. Barbarito, et al., Nucl. Instr. and Meth. A 365 (1995) 214.
[54] I. D'Antone, et al., IEEE, Trans. Nucl. Sci. NS-36 (1989) 1602.
[55] I. D'Antone, et al., IEEE, Trans. Nucl. Sci. NS-41 (1994) 83.
[56] Technical specifications for Ball-Efratom (Irvine, California) Model MRT-H or MRK-S.
[57] http://www.df.unibo.it/macro/pub1.htm.

Glossary

ADC: Analog to Digital Converter.
ASIC: Application Specific Integration Circuit.
Attico: The upper part of MACRO.
CAEN: A company which supplies electronics used in particle physics.
CAMAC: An electronics packaging and signal size standard.
CES: Name of an electronics company.
CR39: A type of plastic useful for track-etch particle detection.
CSGA: A CAMAC routine for block transfers.
CSR: Special memory in the VIC8250 for page descriptor information.
CVAX: A microprocessor in the KAV30 single-board computer.
DIGOR: Digital OR.
DISCAL: The digital electronics module used by the TRD system.
DIP: Dual Inline Package.
DMA: Direct Memory Access.
DSM: Double Super Module.
ERP: Energy Reconstruction Processor.
ESONE: European Studies on Norms for Electronics; an electronics standard.
Ethernet: A protocol for data exchange between computers.
EVD: Event Display program.
FADC: Flash ADC.
FIFO: First In First Out.
FMT: Fast Monopole Trigger.
FPT: Fast Particle Trigger.
FWHM: Full Width at Half Max.
GPS: Global Positioning System.
HCT: High Charge Trigger.
HIPT: Highly Ionizing Particle Trigger.
HV: High Voltage.
KAV30: A Digital Equipment Corp microcomputer.
LAN: Local Area Network.
LeCroy: A company supplying electronics for particle physics.
LI: Leaky Integrator.
LIP: Lightly Ionizing Particles.
LNGS: The Gran Sasso National Laboratory.
MACRO: Monopole, Astrophysics, and Cosmic Ray Observatory.
NIM: An electronics packaging and signal size standard.
PHRASE: Pulse Height Recorder and Synchronous Encoder.
PMT: Photomultiplier Tube.
PPS: Precise Time Pulses from the GPS receiver.
QTP: Charge and Time Processor.
RAM: Random Access Memory.
REL: Restricted Energy Loss.
SM: Super Module.
SMT: Slow Monopole Trigger.
ST: Streamer Tube(s).
STAS: Streamer Tube Acquisition System.
TDC: Time to Digital Converter.
TOF: Time of Flight.
TOHM: Time-Over-Half-Maximum.
TRD: Transition Radiation Detector.
VAX: A Digital Equipment Corp computer product.
VAXELN: Real-time software system.
VME: An electronics hardware/software standard.
VMV: A bus protocol.
WFD: Wave Form Digitizer(s).
WIMP: Weakly Interacting Massive Particle.
WSM: WFD Stop Master.